An Augmented Lagrangian Method for Complex-Valued Compressed SAR Imaging

H. Emre Güven, Alper Güngör, and Müjdat Çetin

***Abstract*—In this paper, we present a solution to the complex synthetic aperture radar (SAR) imaging problem within a constrained optimization formulation where the objective function includes a combination of the ℓ_1-norm and the total variation of the magnitude of the complex valued reflectivity field. The technique we present relies on recent advances in the solution of optimization problems, based on Augmented Lagrangian Methods, and in particular on the Alternating Direction Method of Multipliers (ADMM). We rigorously derive the proximal mapping operators, associated with a linear transform of the magnitude of the reflectivity vector and magnitude-total-variation cost functions, for complex-valued SAR images, and thus enable the use of ADMM techniques to obtain computationally efficient solutions for radar imaging. We study the proposed techniques with multiple features (sparse and piecewise-constant in magnitude) based on a weighted sum of the 1-norm and magnitude-total-variation. We derive a fast implementation of the algorithm using only two transforms per iteration for problems admitting unitary transforms as forward models. Experimental results on real data from TerraSAR-X and SARPER—airborne SAR system developed by ASELSAN—demonstrate the effectiveness of the proposed approach.**

I. Introduction

In this paper we consider the problem of compressed synthetic aperture radar (SAR) imaging using an augmented Lagrangian approach to solve the optimization problem associated with the SAR observation model. There exist several sparsity-driven techniques in the context of SAR imaging [1]–[8], though an important factor hindering their use in practice is the excessively high computational cost of solving the associated optimization problem. From this standpoint, it is important to incorporate recent advances in optimization techniques. The motivation for our work stems from the need to employ computationally efficient algorithms for compressed sensing in SAR, with a potential for parallel implementation.

Some of the current approaches for Compressive SAR imaging include separating real and imaginary parts of the reflectivity field vector [1] and defining a cost function based on the magnitude of the reflectivity field [3], [9]. For reconstruction, while [9] adopts an analysis based approach and uses a particular quasi-Newton algorithm, [3] adopts a synthesis based objective function and uses the spectral projected gradient algorithm [10] to reconstruct the reflectivity field. [5] also uses a synthesis-based approach with a quasi-Newton algorithm for reconstruction. In [11], an adaptive sequential basis selection strategy is employed for point-enhanced imaging. [8] and [12] employ greedy algorithms for computational efficiency. For a review of greedy methods for compressed sensing, see [13].

Alternating Direction Method of Multipliers (ADMM) techniques have been successfully applied to signal and image recovery problems [14]–[19]. ADMM provides a divide-and-conquer approach by splitting unconstrained multi-objective convex optimization problems, augmenting the Lagrangian of the convex optimization problem with a norm-squared error term, and using a non-linear block Gauss-Seidel approach on the resultant terms in the optimization problem. The resulting algorithm is guaranteed to converge under mild conditions [16], [17].

In this paper, we provide a framework for the application of an improved version of a particular ADMM, namely the Constrained Split Augmented Lagrangian Shrinkage Algorithm (C-SALSA) [17] to SAR imaging; introduce a method to handle complex SAR imagery in the constrained total variation minimization (TVM) formulation, where the cost function involves the total variation (TV) of the reflectivity magnitudes. To this end, we derive the proximal mappings of these cost functions involving complex-valued arguments. We use a formulation enabling the use of cost functions with weighted sums of the TV and ℓ_1-norm of reflectivity magnitudes, for which case we present a particular ADMM algorithm. Preliminary versions of the approach proposed here can be found in [20], [21]. However, here we present a generalized version of the algorithm, derivation of proximal mappings for complex-valued imaging, and a comprehensive experimental analysis on SAR imaging of large natural scenes.

The proposed techniques enable the use of ADMM for complex SAR imaging with multiple features. Experimental results on real data from TerraSAR [22] and SARPER [23]—airborne SAR system developed by ASELSAN—demonstrate the effectiveness of the proposed approach and perform well regarding computation time, increasing the potential for employment in practical SAR systems.

II. Background

In this section, we provide some brief background on the measurement model in SAR imaging, feature-enhanced sparse imaging techniques, and augmented Lagrangian methods.

Manuscript received December 02, 2015; revised April 05, 2016; accepted May 30, 2016. Date of publication June 13, 2016; date of current version August 05, 2016. This work was supported in part by The Scientific and Technological Research Council of Turkey and in part by the Undersecretariat for Defense Industries (SSM). The associate editor coordinating the review of this manuscript and approving it for publication was Prof. Oliver Cossairt.

H. E. Güven and A. Güngör are with the ASELSAN A.Ş., Ankara 06172, Turkey (e-mail: heguven@aselsan.com.tr; alpergungor@aselsan.com.tr).

M. Çetin is with the Faculty of Engineering and Natural Sciences, Sabancı University, Istanbul 34956 Turkey (e-mail: mcetin@sabanciuniv.edu).

Color versions of one or more of the figures in this paper are available online at http://ieeexplore.ieee.org.

Digital Object Identifier 10.1109/TCI.2016.2580498

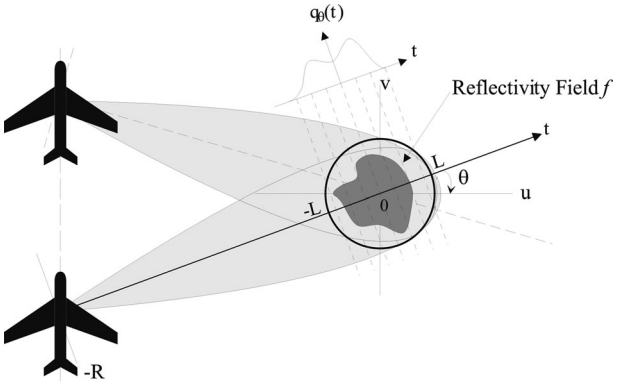

Fig. 1. Spotlight mode SAR geometry [9]

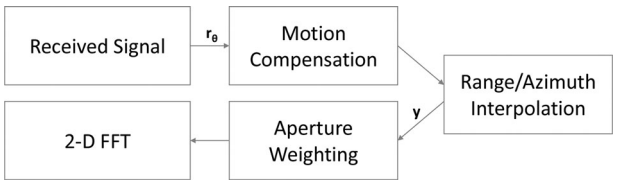

Fig. 2. Typical processing steps for conventional SAR image formation

A. Notation

Regarding the notation used in the paper, the images we work on are stacked as complex-valued column vectors, denoted with bold letters such as $\mathbf{x}, \mathbf{y}, \mathbf{z}$. Subscript denotes the iteration count, i.e., $\mathbf{x}_k$ for the value of $\mathbf{x}$ at the k-th iteration. For operations regarding elements of vectors, $\mathbf{x}[i]$ denotes the i-th element of the vector. However, since we work with TV defined in two dimensions, we use $\mathbf{x}[i,j]$ to denote the i,j-th pixel of the image, and the $(iN_v + j)$-th element of the vector $\mathbf{x}$, where each vertical line in the image bears N_v pixels.

B. SAR Observation Model

The observation geometry for spotlight mode SAR is shown in Fig. 1 [9]. A radar transverses a flightpath, and transmits high-bandwidth pulses at equal angular increments. The received pulses constitute the signal as in the following equation:

$$r_\theta = \iint_{u^2+v^2 \le L^2} f(u,v) \exp\{-j\Omega(ucos\theta + vsin\theta)\} dudv, \tag{1}$$

where f is the underlying reflectivity field, θ is the angle between the u and t axes in Fig. 1, and Ω serves as the radial spatial frequency. Then, projection-slice theorem can be used to identify the received signal as the Fourier transform of the projections of the field [24]–[28]. In this paper, we assume that the spotlight data is used to interpolate the samples in the two-dimensional (2-D) Fourier transform domain, which we consider as the measurement vector $\mathbf{y}$. Motion compensation in Fig. 2 depicts the process of correcting residual effects from the received signal due to non-ideal motion. Range/Azimuth interpolation is the process of interpolating data onto cartesian grid. Also, to correct errors due to non-ideal propagation media and non-ideal motion compensation, an optional autofocusing step is applied after forming the image. For further details on SAR imaging, the interested reader may refer to many useful texts including [24]–[26].

Hence, the SAR observation model can be considered linear in relating the vector containing the SAR image pixels to the data vector, e.g., consisting of phase history data for spotlight mode SAR imaging. Let us denote the image vector to be constructed by sequentially indexed pixel-values $\mathbf{x} \in \mathbf{C}^N$ and observation kernel by the matrix $\mathbf{B} \in \mathbf{C}^{M \times N}$, which relates $\mathbf{x}$ to the measurement vector $\mathbf{y} \in \mathbf{C}^M$:

$$\mathbf{y} = \mathbf{B}\mathbf{x} + \mathbf{n}, \tag{2}$$

where $\mathbf{n} \in \mathbf{C}^M$ is the additive noise vector, typically from a normal distribution. The data vector $\mathbf{y}$ can lie in the phase history domain, in which case the matrix $\mathbf{B}$ would be a spatial Fourier transform operator; or $\mathbf{y}$ can be a conventionally reconstructed image, in which case $\mathbf{B}$ would be a convolution operator associated with the point spread function of the entire imaging process.

In this paper, to exploit the speed of Fourier transform on a Cartesian grid, the data are assumed to be in the phase history domain [24], and pre-compensated for platform motion. Then the data are interpolated onto a Cartesian grid to use the polar format algorithm, which addresses the issue of range cell migration. The matrix $\mathbf{B}$ is simply a masked Fourier Transform operator, which can be written as the multiplication of the data selection matrix $\mathbf{M} \in \mathbf{R}^{M \times N}$ with the Fourier Transform Matrix $\mathbf{U} \in \mathbf{R}^{N \times N}$, i.e., $\mathbf{B} = \mathbf{M}\mathbf{U}$. In the reconstruction algorithms we use, however, the matrix associated with the Fourier operator is never formed explicitly. Instead, 2-D FFTs are used to perform the associated matrix-vector products. For wide-angle [38] or near-field SAR imaging, associated models can be used at their respective cost, although these details are beyond the scope of our work.

C. Feature Enhanced Imaging

The sparsity driven SAR imaging problem can be cast as

$$\underset{\mathbf{x}}{\text{minimize}} \ \|\mathbf{B}\mathbf{x} - \mathbf{y}\|_2^2 + \lambda\phi(\mathbf{x}), \tag{3}$$

where $\phi(\mathbf{x})$ is the penalty function appropriately selected according to the reflectivity characteristics of the region to be imaged. An alternative form is the constrained problem:

$$\begin{array}{ll} \underset{\mathbf{x}}{\text{minimize}} & \phi(\mathbf{x}) \\ \text{subject to} & \|\mathbf{B}\mathbf{x} - \mathbf{y}\|_2 \le \epsilon \end{array}, \tag{4}$$

where the error norm is prescribed to be smaller than a radius ϵ suggested by the signal-to-noise ratio (SNR) that can be estimated from the data. Such an estimation can be performed relatively more easily in SAR imaging scenarios, for instance, by collecting measurements before transmitting a radar pulse solely for the purpose of obtaining noise samples. Thus, we prefer the constrained form (4) over (3), although the proximal mappings presented in the next section can be used in either form of the problem. Depending on the selection of the penalty

function $\phi(\mathbf{x})$, the characteristics of the reconstruction varies. In what follows, we consider the special cases with the 1-norm $\|\mathbf{x}\|_1$ and the TV of the image magnitude $TV(|\mathbf{x}|)$.

1) 1-Norm Enhanced Imaging: $\phi(\mathbf{x}) = \|\mathbf{x}\|_1$ results in the enhancement of sparsity in the image domain. The use of 1-norm as a penalty function has a long history in the solution of inverse problems. In SAR imaging, it has been shown to enhance strong scatterers in a weak background [9]. Compressed sensing literature has shown that, given sufficient measurements obtained using an incoherent basis, minimizing the 1-norm closely approximates finding the sparsest solution possible. Therefore, this penalty function is appropriate for obtaining images with higher resolution in cases with sparse scenery [9].

2) TV Enhanced Imaging: $\phi(\mathbf{x}) = TV(|\mathbf{x}|)$ results in reconstructions with emphasized piecewise-constant features, $TV(|\mathbf{x}|)$ being the TV of magnitude of the complex-valued image to be reconstructed [9], [17]. It is important to note that SAR images are complex and we choose to apply the TV on the magnitude of the SAR image. TV is known to reduce speckle noise in images [9], [29]. By applying TV on the magnitude of the reflectivity field, we aim to reconstruct speckle suppressed images. The handling of complex SAR data requires special care, as will be described in the sequel.

For an overview of recent work on the use of such sparsity-enforcing methods in SAR imaging, see [4].

D. Augmented Lagrangian Methods (ALMs) for Imaging

ALMs approach constrained optimization problems by adding a penalty term to the Lagrangian that is zero for any feasible vector, which enables convergence under far more general conditions [14]. ADMM, a particular form of ALMs, provides a divide-and-conquer approach by splitting the primal variables to obtain separability in the Augmented Lagrangian, and performing sequential updates that are simpler to implement. Algorithm 1 shows the steps of the ADMM for solving problems of type (3) by Variable Splitting [16] and alternating the optimization variable in sub-problems. For instance, setting $f_1(\mathbf{x}) = \|\mathbf{B}\mathbf{x} - \mathbf{y}\|_2^2$, $\mathbf{G} = \mathbf{I}$, and $f_2 = \lambda\phi(\mathbf{x})$ in Algorithm 1 yields the solution to problem (3), with steps that can be efficiently implemented [16].

SALSA [16] and C-SALSA [17] are ADMM techniques for image recovery problems that benefit from the augmented Lagrangian and variable splitting to efficiently solve problems of the form (3) and (4), respectively. While there are different approaches in literature [30]–[32] for selection of λ in (3), these techniques generally involve solving (3) many times, thus multiplying the associated computational cost by the number of trials for different values of λ. As parameter selection is somewhat easier in the constrained form (4), we focus on the solution of constrained problems in this paper. The problem in (4) with $\phi(\mathbf{x}) = \|\mathbf{x}\|_1$ can be expressed in an unconstrained form as [17]:

$$\underset{\mathbf{x}}{\text{minimize}}\ \|\mathbf{x}\|_1 + \iota_{E(\epsilon,\mathbf{I},\mathbf{y})}(\mathbf{B}\mathbf{x}), \tag{5}$$

Algorithm 1: *ADMM*ADMM [17]

1.Set $k = 0$, choose $\mu > 0$, $\mathbf{z}_0$, $\mathbf{d}_0$

2.**repeat**

3.$\mathbf{x}_{k+1} = \arg\min_{\mathbf{x}}\ f_1(\mathbf{x}) + \frac{\mu}{2}\|(\mathbf{G}\mathbf{x} - \mathbf{z}_k - \mathbf{d}_k)\|_2^2$

4.$\mathbf{z}_{k+1} = \arg\min_{\mathbf{z}}\ f_2(\mathbf{z}) + \frac{\mu}{2}\|(\mathbf{G}\mathbf{x}_{\mathbf{k+1}} - \mathbf{z} - \mathbf{d}_k)\|_2^2$

5.$\mathbf{d}_{k+1} = \mathbf{d}_k - \mathbf{G}\mathbf{x}_{\mathbf{k+1}} + \mathbf{z}_{k+1}$

6.$k \leftarrow k + 1$

7.**until** some stopping criterion is satisfied.

where $\iota_{E(\epsilon,\mathbf{I},\mathbf{y})}(\mathbf{B}\mathbf{x})$ is the indicator function of the feasible set $E(\epsilon, \mathbf{I}, \mathbf{y})$ such that:

$$E(\epsilon, \mathbf{A}, \mathbf{y}) = \left\{\mathbf{x} \in \mathbf{C}^N : \|\mathbf{A}\mathbf{x} - \mathbf{y}\|_2 \le \epsilon\right\}, \tag{6}$$

$$\iota_S(\mathbf{s}) = \begin{cases} 0, & \text{if } \mathbf{s} \in S \\ +\infty, & \text{if } \mathbf{s} \notin S \end{cases}. \tag{7}$$

The steps of C-SALSA are shown in Algorithm 2. The vectors $\mathbf{z}_0^{(1)}$ and $\mathbf{d}_0^{(1)}$ are in $\mathbf{C}^N$, whereas $\mathbf{z}_0^{(2)}$ and $\mathbf{d}_0^{(2)}$ are in $\mathbf{C}^M$. The operators $\mathbf{\Psi}_{\phi/\mu}$ and $\mathbf{\Psi}_{\iota_{E(\epsilon,\mathbf{I},\mathbf{y})}}$ are the Moreau proximal mappings for $\frac{1}{\mu}\phi(\mathbf{x}) = \frac{\|\mathbf{x}\|_1}{\mu}$ and $\iota_{E(\epsilon,\mathbf{I},\mathbf{y})}(s)$, and are given by

$$\mathbf{\Psi}_{\phi/\mu}(\mathbf{s}) = \text{soft}(\mathbf{y}, 1/\mu), \tag{8}$$

and

$$\mathbf{\Psi}_{\iota_{E(\epsilon,\mathbf{I},\mathbf{y})}}(\mathbf{s}) = \begin{cases} \mathbf{s}, & \text{if } \|\mathbf{s} - \mathbf{y}\|_2 \le \epsilon \\ \mathbf{y} + \epsilon\frac{(\mathbf{s}-\mathbf{y})}{\|\mathbf{s}-\mathbf{y}\|_2}, & \text{if } \|\mathbf{s} - \mathbf{y}\|_2 > \epsilon \end{cases}, \tag{9}$$

respectively, where $\text{soft}(\mathbf{y}, \tau)$ denotes the element-wise application of the soft-thresholding function

$$y \mapsto \text{sign}(y) \cdot \max\{|y| - \tau, 0\}, \tag{10}$$

for real vectors [17]. In recovery of real images with the TVM formulation, $\Psi_{\phi/\mu}$ can be performed using Chambolle projections [33] to obtain the corresponding Moreau proximal mappings [17].

III. Complex SAR Imaging Using ALMs

In this section, we first consider the problem of handling phase in the context of complex-valued SAR imaging and present the proximal mapping functions associated with the 1-norm of a linear transformation as well as with the TV of the reflectivity magnitudes. Next, we generalize the problem and consider the use of hybrid (1-norm plus TV of the magnitude) cost functions and present an ADMM algorithm for this general case.

A. Handling Phase for Complex Imaging

The Moreau proximal mapping for ϕ is defined as:

$$\text{prox}_\phi(\mathbf{v}) = \arg\min_{\mathbf{x}}\ \phi(\mathbf{x}) + \frac{\mu}{2}\|\mathbf{x} - \mathbf{v}\|_2^2. \tag{11}$$

We consider setting the cost function to 1-norm of a sparsifying linear transformation of the magnitudes, $\phi(\mathbf{x}) = \|\mathbf{W}|\mathbf{x}|\|_1$.

Some transforms that can be used to sparsify natural images include wavelet and discrete cosine transforms. However, these transformations should be applied on the magnitude of the reflectivity field. Hence proximal mappings need to be extended to handle complex case. Theorem 1 below defines a generalized Moreau proximal mapping for a cost function $\phi(\mathbf{x}) = \|\mathbf{W}|\mathbf{x}|\|_1$, that is the 1-norm of a linear transformation $\mathbf{W}|\mathbf{x}|$ of the vector of absolute values $|\mathbf{x}|$ of the complex vector $\mathbf{x} \in \mathbf{C}^N$.

Theorem 1: Let $\phi(\mathbf{x}) = \|\mathbf{W}|\mathbf{x}|\|_1$ for $\mathbf{x} \in \mathbf{C}^N$, then $\text{prox}_{\phi}(\mathbf{v}) = \text{prox}_{\|\mathbf{W}\mathbf{x}\|_1}(|\mathbf{v}|) \cdot \exp\{\text{j}\angle(\mathbf{v})\}$.

For $\phi(\mathbf{x}) = \|\mathbf{x}\|_1$, an appropriate choice of the cost function for complex images sparse in the spatial domain, the associated Moreau proximal mapping is an extended version of the soft thresholding mapping defined for real vectors. In particular, setting $\mathbf{W} = \mathbf{I}$ yields the proximal mapping function for ℓ_1-norm as $\text{soft}(|\mathbf{y}|, \tau) \exp\{\text{j}\angle\mathbf{y}\}$. The proof for the more general case in Theorem 1 can be found in Appendix A. Also, a special case of this proof is given for ℓ_1-norm in [34].

It is well-known that the TV is a more suitable cost function for image components with piecewise-constant characteristics to use within the constrained optimization formulation (4). For recovering real-valued images with the TVM formulation, $\Psi_{\phi/\mu}$ can be performed using Chambolle projections to obtain the corresponding Moreau proximal mappings. However, handling of phase requires further care, especially in the isotropic TVM formulation for complex-valued vectors $\mathbf{x}$, which is not covered by Theorem 1. As in the context of SAR imaging, it is important to incorporate the fact that the field of reflectivity magnitudes may be piecewise-constant, while the phase thereof may vary randomly in each pixel. As such, the cost function $\phi(\mathbf{x})$ in (4) should be selected as:

$$TV\left(|\mathbf{x}|\right) = \sum_{i,j} |\nabla\left(|\mathbf{x}|\right)|[i,j], \tag{12}$$

where

$$|\nabla\left(|\mathbf{x}|\right)|[i,j] = \sqrt{\left(D_h|\mathbf{x}|\right)^2 + \left(D_v|\mathbf{x}|\right)^2}, \tag{13}$$

and

$$\left(D_h|\mathbf{x}|\right) = |\mathbf{x}[i+1,j]| - |\mathbf{x}[i,j]|, \tag{14}$$

$$\left(D_v|\mathbf{x}|\right) = |\mathbf{x}[i,j+1]| - |\mathbf{x}[i,j]|. \tag{15}$$

Here, we extend the use of ADMMs for image recovery to include cases where the objective comprises the magnitude-total-variation $TV(|\cdot|)$ of complex imagery. The TV of the image magnitude given by $\phi(\mathbf{x}) = TV\left(|\mathbf{x}|\right)$ is associated with the Moreau proximal mapping defined in Theorem 2:

Theorem 2: Let $\phi(\mathbf{x}) = TV\left(|\mathbf{x}|\right)$. Then, $\text{prox}_{TV(|\cdot|)}(\mathbf{v})[i,j] = \text{prox}_{TV}\left(|\mathbf{v}|\right)[i,j] \cdot \exp\{\text{j}\angle(\mathbf{v}[i,j])\}$, where $\text{prox}_{TV}(\cdot)$ is the proximal mapping for the TV function $TV(\mathbf{x})$.

The proof can be found in Appendix B.

For real-valued images, it is sufficient to use a fixed number of steps involving Chambolle's projections to account for the Moreau proximal mapping for the TV function [17]. Similarly, for complex-valued images, we apply Chambolle's algorithm for a fixed number of steps on the magnitude of the image, and combine the resulting magnitude with the initial phase at each ADMM iteration. In mathematical terms:

$$\left(\Psi_{TV(|\cdot|)/\mu}(\mathbf{s})\right)[i,j] = \exp\{\text{j}\angle(\mathbf{s}[i,j])\}\left(\Psi_{TV(\cdot)/\mu}(|\mathbf{s}|)\right)[i,j], \tag{16}$$

where $\Psi_{TV(\cdot)/\mu}$ is the Moreau proximal mapping corresponding to the cost function $TV(\cdot)/\mu$, obtained herein using Chambolle projections the same way as in C-SALSA [17].

Conventional isotropic TV is proven to exhibit compressed sensing guarantees [35]. While the proof can not be directly extended to TVM, magnitude regularization has been previously used with success in a compressive imaging framework [36]. Here we acknowledge that traditional compressed sensing guarantees are not currently known to be applicable for the proposed TVM formulation. Still, empirical results suggest it to be suitable and effective for SAR imaging as will be shown in Section IV. Future work in this respect is needed to fill the gap for theoretical guarantees of recovery through nonlinear sparsifying transformations.

The proximal mapping functions defined here allow us to use ADMM for complex SAR imagery with desired cost functions on the magnitudes of the images.

Algorithm 2: *C-SALSA* [17]

1. Set $k = 0$, choose $\mu > 0$, $\mathbf{z}_0^{(1)}$, $\mathbf{z}_0^{(2)}$, $\mathbf{d}_0^{(1)}$, $\mathbf{d}_0^{(2)}$
2. **repeat**
3. $\mathbf{r}_k = \mathbf{z}_k^{(1)} + \mathbf{d}_k^{(1)} + \mathbf{B}^H\left(\mathbf{z}_k^{(2)} + \mathbf{d}_k^{(2)}\right)$
4. $\mathbf{x}_{k+1} = \left(\mathbf{I} + \mathbf{B}^H\mathbf{B}\right)^{-1}\mathbf{r}_k$
5. $\mathbf{z}_{k+1}^{(1)} = \mathbf{\Psi}_{\phi/\mu}\left(\mathbf{x}_{k+1} - \mathbf{d}_k^{(1)}\right)$
6. $\mathbf{z}_{k+1}^{(2)} = \mathbf{\Psi}_{\iota_{E(\epsilon,\mathbf{I},\mathbf{y})}}\left(\mathbf{B}\mathbf{x}_{k+1} - \mathbf{d}_k^{(2)}\right)$
7. $\mathbf{d}_{k+1}^{(1)} = \mathbf{d}_k^{(1)} - \mathbf{x}_{k+1} + \mathbf{z}_{k+1}^{(1)}$
8. $\mathbf{d}_{k+1}^{(2)} = \mathbf{d}_k^{(2)} - \mathbf{B}\mathbf{x}_{k+1} + \mathbf{z}_{k+1}^{(2)}$
9. $k \leftarrow k+1$
10. **until** some stopping criterion is satisfied.

B. ADMM for Constrained Optimization With a Hybrid Cost Function

A critical aspect of feature enhanced SAR imaging, and compressed sensing methods alike, is the proper selection of the sparsifying transform. While 1-norm minimization in the image domain tends to work well for strong scatterers in a weakly scattering background, TV of the image magnitude performs better for profiles with piecewise constant features. Nonetheless, natural scenes are usually a composition of sparse and piecewise-constant scattering characteristics [9]. In practice, it is essential to account for various scattering profiles present in the region of interest for imaging, as it has been successfully used in sparsity based SAR imaging [3], [9], [21], [37]. As such,

we propose to use a hybrid cost function in the ADMM formulation, in particular, a weighted sum of the 1-norm and the TV of the image magnitude.

In particular, we use a solution to the constrained optimization problem with a hybrid cost function, by separating the weighted components in the augmented Lagrangian, starting from the general ADMM framework given in Algorithm 1. Specifically, in order to solve the optimization problem of the form:

$$\begin{array}{ll} \underset{\mathbf{x}}{\text{minimize}} & \alpha_1 \phi_1\left(\mathbf{x}\right) + \cdots + \alpha_m \phi_m\left(\mathbf{x}\right) \\ \text{subject to} & \|\mathbf{Bx}-\mathbf{y}\|_2 \leq \epsilon \end{array}, \tag{17}$$

for m separable objective functions. We employ the variable splitting scheme used in [16], [17], by introducing the concatenated variables:

$$\mathbf{z} = \left[\mathbf{z^{(0)}}\ \mathbf{z^{(1)}}\ \cdots\ \mathbf{z^{(m)}}\right]^{\mathbf{T}}, \quad \mathbf{G} = \left[\mathbf{B^T}\ \mathbf{I}\ \cdots\ \mathbf{I}\right]^{\mathbf{T}}, \tag{18}$$

for the transformed problem:

$$\begin{array}{ll} \underset{\mathbf{x}}{\text{minimize}} & f_1(\mathbf{x}) + f_2(\mathbf{z}) \\ \text{subject to} & \mathbf{Px}+\mathbf{Qz}-\mathbf{s}=0 \end{array}. \tag{19}$$

Let us set $\mathbf{P}=\mathbf{G}, \mathbf{Q}=-\mathbf{I}, \mathbf{s}=0, f_1(\mathbf{x})=0$, and

$$f_2(\mathbf{z}) = \iota_{E(\epsilon,\mathbf{I},\mathbf{y})}\left(\mathbf{z^{(0)}}\right) + \sum_{i=1}^{m} \alpha_i \phi_i\left(\mathbf{z^{(i)}}\right), \tag{20}$$

where $\iota_{E(\epsilon,\mathbf{I},\mathbf{y})}\left(\mathbf{z^{(0)}}\right)$ accounts for the indicator function associated with the data fidelity constraint $\|\mathbf{Bx}-\mathbf{y}\|_2 \leq \epsilon$. This setting ensures that $\mathbf{Gx}=\mathbf{z}$, and consequently: $\mathbf{x}=\mathbf{z^{(1)}}=\cdots=\mathbf{z^{(m)}}, \mathbf{Bx}=\mathbf{z^{(0)}}$. The resulting ADMM steps are:

$$\mathbf{x}_{k+1} = \arg\min_{\mathbf{x}} \frac{\mu}{2}\left(\|\mathbf{Gx}-\mathbf{z}_k-\mathbf{d}_k\|_2^2\right) \tag{21}$$

$$\mathbf{z}_{k+1} = \arg\min_{\mathbf{z}} f_2(\mathbf{z}) + \frac{\mu}{2}\|\left(\mathbf{Gx}_{k+1}-\mathbf{z}-\mathbf{d}_k\right)\|_2^2 \tag{22}$$

$$\mathbf{d}_{k+1} = \mathbf{d}_k - \mathbf{Gx}_{k+1} + \mathbf{z}_{k+1}. \tag{23}$$

where Eq. (21) involves a quadratic cost and leads to a closed-form solution:

$$\mathbf{x}_{k+1} = (\mathbf{G}^H\mathbf{G})^{-1}\mathbf{G}^H(\mathbf{d}_k+\mathbf{z}_k) \tag{24}$$

$$= \left(m\mathbf{I}+\mathbf{B^H B}\right)^{-1}\left[\sum_{i=1}^{m}\mathbf{d}_k^{(i)}+\mathbf{z}_k^{(i)}+\mathbf{B}^H\left(\mathbf{d}_k^{(0)}+\mathbf{z}_k^{(0)}\right)\right]. \tag{25}$$

Efficient solutions of Eq. (25) can be obtained using the Woodbury matrix identity [17], such as in the case where $\mathbf{B}$ represents the matrix associated with the observation of partial Fourier transform data with $\mathbf{BB}^H=\mathbf{I}$, so that:

$$(m\mathbf{I}+\mathbf{B^H B})^{-1} = \frac{1}{m}(\mathbf{I}-\frac{1}{m+1}\mathbf{B}^H\mathbf{B}). \tag{26}$$

Algorithm 3: *ADMM with Hybrid cost function*

1.Set $k=0$, choose $\mu>0$, $\mathbf{z}_0^{(i)}$, $\mathbf{d}_0^{(i)}$, α_i for all i

2.**repeat**

3.$\mathbf{x}_{k+1} = (m\mathbf{I}+\mathbf{B^H B})^{-1}\left[\sum_{i=1}^{m}\mathbf{d}_k^{(i)}+\mathbf{z}_k^{(i)} + \mathbf{B}^H\left(\mathbf{d}_k^{(0)}+\mathbf{z}_k^{(0)}\right)\right]$

4.**for i** $= \mathbf{1}\cdots\mathbf{m}$

5.$\mathbf{z}_{k+1}^{(i)} = \mathbf{\Psi}_{\phi_i \frac{\alpha_i}{\mu}}\left(\mathbf{x}_{k+1}-\mathbf{d}_k^{(i)}\right)$

6.$\mathbf{d}_{k+1}^{(i)} = \mathbf{d}_k^{(i)} - \mathbf{x_{k+1}} + \mathbf{z}_{k+1}^{(i)}$

7.**endfor**

8.$\mathbf{z}_{k+1}^{(0)} = \mathbf{\Psi}_{\iota_{E(\epsilon,\mathbf{I},\mathbf{y})}}\left(\mathbf{Bx}-\mathbf{d}^{(0)}\right)$

9.$\mathbf{d}_{k+1}^{(0)} = \mathbf{d}_k^{(0)} - \mathbf{Bx_{k+1}} + \mathbf{z}_{k+1}^{(0)}$

10.$k \leftarrow k+1$

11.**until** some stopping criterion is satisfied.

In order to solve Eq. (22), the second step in the ADMM, we can use the variable splitting scheme [16], [17], to obtain:

$$\mathbf{z}_{k+1}^{(i)} = \arg\min_{\mathbf{z}^{(i)}} \phi_i\left(\mathbf{z}^{(i)}\right) + \frac{\mu}{2\alpha_i}\left(\|\mathbf{x}_{k+1}-\mathbf{z}^{(i)}-\mathbf{d}_k^{(i)}\|_2^2\right), \text{for } i=1\cdots m \tag{27}$$

$$\mathbf{z}_{k+1}^{(0)} = \arg\min_{\mathbf{z}^{(0)}} \iota_{E(\epsilon,\mathbf{I},\mathbf{y})}\left(\mathbf{z}^{(0)}\right) + \frac{\mu}{2}\left(\|\mathbf{Bx}_{k+1}-\mathbf{z}^{(0)}-\mathbf{d}_k^{(0)}\|_2^2\right). \tag{28}$$

Equation (27) can be recognized as the Moreau proximal mapping $\mathbf{\Psi}_{\frac{\alpha_i}{\mu}\phi_i}\left(\mathbf{x}_{k+1}-\mathbf{d}_k^{(i)}\right)$ associated with function ϕ_i. Equation (28) has a simple solution given by the orthogonal projection $\mathbf{\Psi}_{\iota_{E(\epsilon,\mathbf{I},\mathbf{y})}}\left(\mathbf{Bx}_k-\mathbf{d}_k^{(0)}\right)$ onto the ϵ-radius hypersphere centered at $\mathbf{y}$ [17].

The last step of the ADMM, shown in Eq. (23), simply consists of the updates:

$$\mathbf{d}_{k+1}^{(i)} = \mathbf{d}_k^{(i)} - \mathbf{x}_{k+1} + \mathbf{z}_{k+1}^{(i)}, \text{for } i=1\cdots m \tag{29}$$

$$\mathbf{d}_{k+1}^{(0)} = \mathbf{d}_k^{(0)} - \mathbf{Bx}_{k+1} + \mathbf{z}_{k+1}^{(0)}. \tag{30}$$

With these substitutions, the ADMM solution we propose for problem (17) is given in Algorithm 3. We have chosen $m=2$, the two cost functions as $\phi_1(\cdot)=\|\cdot\|_1$ and $\phi_2(\cdot)=TV\left(|\cdot|\right)$ for our experimental results in Section IV. Even though Algorithm 3 can be viewed as an instantiation of the general algorithm *ADMM-2* in [17], the specified cost functions and transformations in problem (19) and Eq. (20) require adjustments given in the above steps for completeness. Also, the solution here includes the fast solution of step 3 given in Eq. (26), as we describe in the next section.

C. Fast Solution of Proposed Approach For Unitary Transform Domains

When the gathered data are in a unitary transform domain as in our case, the proposed approach can be solved using only one forward and one inverse transform per iteration. This includes the fast calculation of $\mathbf{x}_{k+1}$ and $\mathbf{B}\mathbf{x}_{k+1}$ vectors as described below.

Using $\mathbf{B} = \mathbf{M}\mathbf{U}$, $\mathbf{U}\mathbf{U}^H = \mathbf{I}$ and $\mathbf{M}\mathbf{M}^H = \mathbf{I}$, where $\mathbf{M}$ denotes the masking matrix and $\mathbf{U}$ denotes the unitary transform matrix, we can conclude that $\mathbf{B}\mathbf{B}^H = \mathbf{I}$. Define a slack variable $\mathbf{q}_k$ as

$$\mathbf{q}_k = \sum_{i=1}^{m} \mathbf{d}_k^{(i)} + \mathbf{z}_k^{(i)}. \tag{31}$$

Then, the updated step 3 of the algorithm can be re-written as

$$\mathbf{x}_{k+1} = \frac{1}{m}(\mathbf{I} - \frac{1}{m+1}\mathbf{B}^{\mathbf{H}}\mathbf{B})\left[\mathbf{q}_k + \mathbf{B}^H\left(\mathbf{d}_k^{(0)} + \mathbf{z}_k^{(0)}\right)\right], \tag{32}$$

$$\mathbf{x}_{k+1} = \frac{1}{m}\left[\mathbf{q}_k + \frac{1}{m+1}\mathbf{B}^H\left(m\left(\mathbf{d}_k^{(0)} + \mathbf{z}_k^{(0)}\right) - \mathbf{B}\mathbf{q}_k\right)\right]. \tag{33}$$

Then, $\mathbf{B}\mathbf{x}_{k+1}$ can be calculated as

$$\mathbf{B}\mathbf{x}_{k+1} = \frac{1}{m+1}\left[\mathbf{B}\mathbf{q}_k + \left(\mathbf{d}_k^{(0)} + \mathbf{z}_k^{(0)}\right)\right]. \tag{34}$$

Therefore, besides proximal mapping functions, the algorithm can be carried out using only one forward and one inverse transform per iteration. Since Fourier transform is unitary, this can be applied to SAR imaging directly using the method described in Section II. The implication of this is that this algorithm now has the computational efficiency of greedy methods such as orthogonal matching pursuit [39]. In the next section, we study the performance of Algorithm 3 with numerical examples, as well as real SAR data.

IV. Experimental Results

In this section, we present several examples illustrating the performance of the augmented Lagrangian approach for complex SAR imaging. For the examples with TerraSAR [22], we form the phase history data from reference SAR images obtained from full-angle, full-bandwidth SAR returns; while we use complex (I/Q) data in the phase history domain for experiments with SARPER—airborne SAR system developed by ASELSAN. In the implementation of Algorithm 3, the ADMM parameter μ is multiplied by a scalar larger than 1 at each iteration, as is suggested in [14], [17], in this case by a factor of 1.1 at each iteration starting from a value of 10.

In our first example, in order to illustrate the effectiveness of using magnitude-total-variation as the cost function, we perform a simulation with two rectangular objects on a flat background. For the low-resolution measurement scenario, 25% of the reference samples are maintained in a rectangular region in the 2-D Fourier space at the center of the grid. This scenario is applicable in practice since all practical SAR sensors can be essentially regarded as making observations with a band-limited / narrow-aperture data. Each pixel in the spatial domain is given a uniformly random phase value between 0 and 2π. Fig. 3(a)–(d) show the reference image, the minimum-norm reconstruction with zero-padding beyond the available samples, reconstruction minimizing the TV over real and imaginary parts of the complex SAR image, and lastly our proposed reconstruction by minimizing the TV of the magnitude of the complex SAR image using the proximal mapping defined in Theorem 2. For the proximal mapping function associated with TV, we used five iterations of Chambolle projections [17], [33] in step 5 of Algorithm 3. Clearly, the reconstruction by minimization of the TV of the real and imaginary parts suffers from artifacts due to the spatial phase variation in the complex image, not properly accounted for in this approach. On the other hand, minimizing the magnitude-total-variation results in more accurately represented features in the center, as well as better overall contrast. This example shows that our algorithm performs magnitude-total variation regularization effectively.

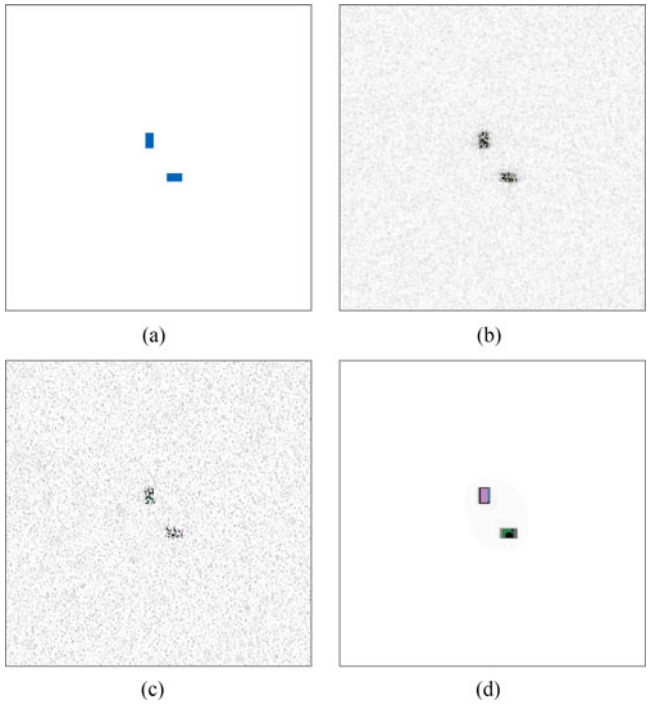

Fig. 3. (a) Reference image. (b) Minimum-norm reconstruction. (c) TV over real/imaginary parts. (d) TVM over magnitude.

Next, we study the performance of the hybrid cost function for different sparsity, SNR, and sampling levels using simulated data. We construct 128×128 random scenes consisting of point and rectangularly-shaped targets (each dimension ≤ 5 pixels wide), and add randomly varying phase. We perform reconstructions for sampling levels of $\{0.2, 0.4, 0.6\}$, and input SNR levels of 30 dB and 10 dB, and measure the performance in terms of peak-signal-to-noise-ratio (pSNR) of the reconstructed images. For each SNR and sampling level, we have run this simulation 100 times with randomly generated scenes corresponding to different sparsity levels. In our analysis of the results, we consider both spatial sparsity as well as reflectivity gradient

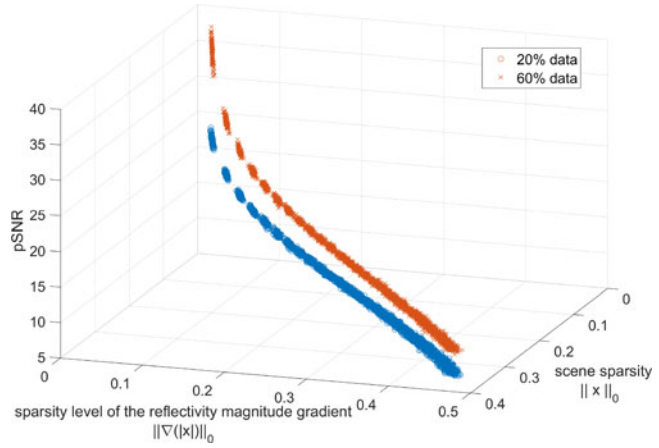

Fig. 4. pSNR versus scene sparsity and sparsity level of the reflectivity magnitude gradient.

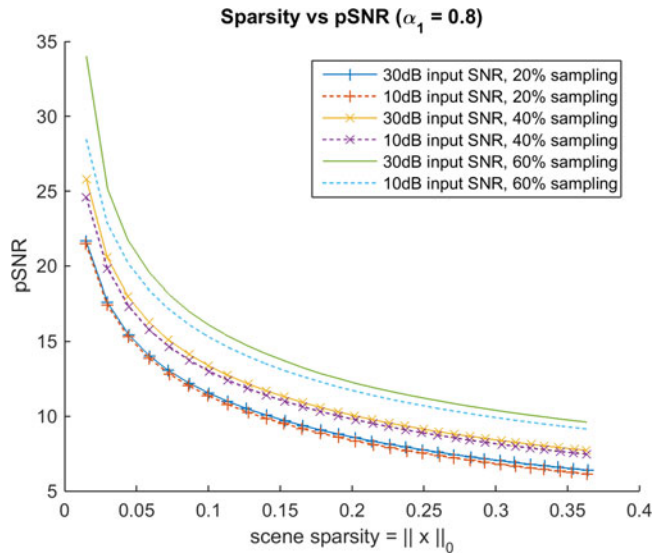

Fig. 5. Projection of the 3d plot onto scene sparsity versus pSNR axes.

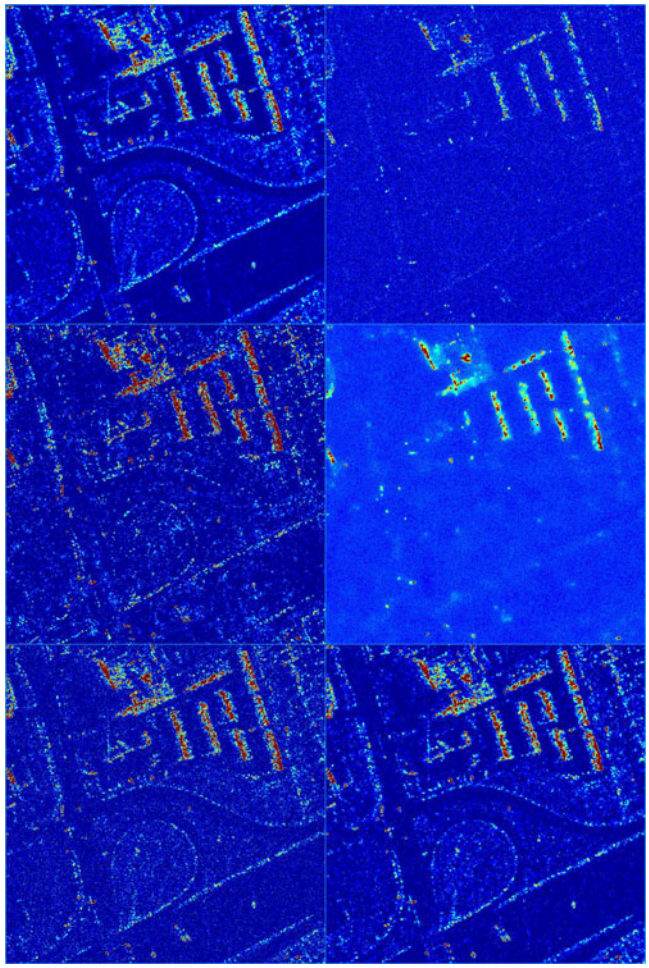

Fig. 6. TerraSAR reference image (top-left), Minimum-norm reconstruction (top-right), Minimum 1-norm reconstruction (middle-left), Minimum magnitude-TV reconstruction (middle-right), Reconstruction with hybrid cost including TV of real and imaginary parts (bottom-left), Proposed reconstruction with hybrid cost including magnitude-TV (bottom-right)

magnitude sparsity. We define the sparsity rates as the ratio of the number of non-zero reflectivities or gradients to the total number of pixels. The plot relating pSNR, scene sparsity, and sparsity level of the reflectivity magnitude gradient can be seen in Fig. 4 for two different sampling levels. Fig. 5 shows the projection of the 3-D plot on pSNR and scene sparsity axes, for different SNR and sampling levels. It is interesting to note that the reconstruction performance is acceptable at practical input SNR levels such as 30 dB and 10 dB. We observe gradual decrease in pSNR as we reduce the number of measurements, add more noise, and make the scene less sparse.

In our next example, we study a TerraSAR [22] image example with sparse features as well as piecewise-constant-magnitude features. The binary random mask in the Fourier space that contains 39% of the samples used for the reference image. Even though completely random sub-sampling is not currently applicable in practice, to show the performance of the algorithm in a scenario involving irregular data limitations, we have used such a setting. For a study of practical sensing and random sub-sampling considerations in mono- and multi-static SAR, see, e.g., [40]. The parameter selection is made as $\alpha_1 = 0.8$ for 1-norm and $\alpha_2 = 0.2$ for the hybrid cost function, although other choices result in different levels of emphasis in each feature associated with the corresponding weight. We observed this choice of weights results in satisfactory imaging performance, although the optimal selection may require a thorough statistical study over a diverse set of SAR images, which is beyond the scope of this paper. Fig. 6 shows the reference image, the minimum-norm reconstruction, and reconstructions with cost functions of 1-norm, magnitude-TV, hybrid-cost with TV over real/imaginary parts and hybrid-cost with magnitude-TV. The contrast across piecewise-constant features appear visually improved by the hybrid cost (with magnitude-TV) relative to the 1-norm reconstruction, while better maintaining super-resolution features compared to the minimum magnitude-TV solution. The hybrid cost minimization including the TV over real/imaginary parts also performs poorly in terms of the contrast and speckle reduction compared to the hybrid cost minimization

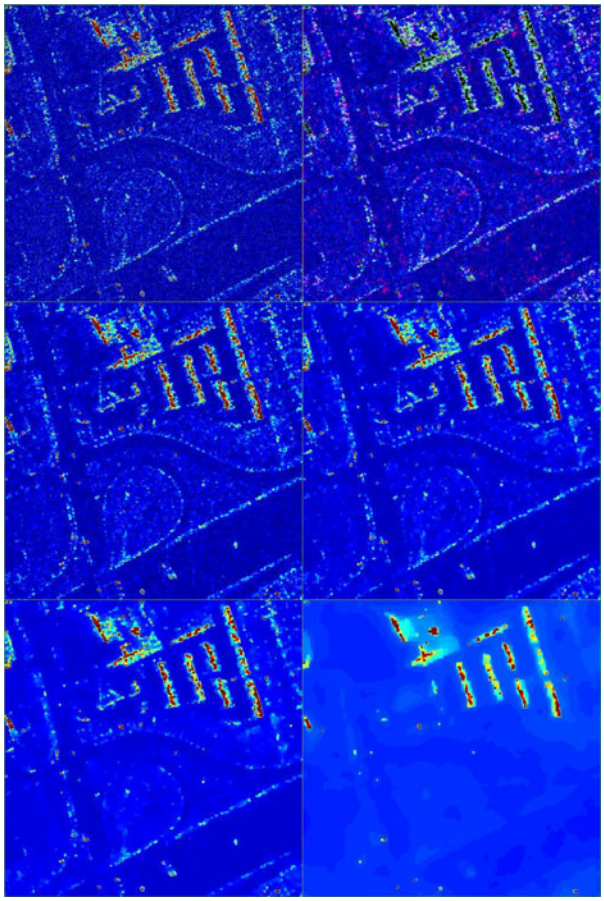

Fig. 7. Proposed reconstruction of TerraSAR images with $\alpha_1 = 0.9$ (top-left), $\alpha_1 = 0.8$ (top-right), $\alpha_1 = 0.7$ (middle-left), $\alpha_1 = 0.6$ (middle-right), $\alpha_1 = 0.5$ (bottom-left), $\alpha_1 = 0.2$ (bottom-right). In each case ($\alpha_2 = 1 - \alpha_1$)

including magnitude-TV. This example also verifies that natural scenes with a composition of more than one type of scatterer characteristics [37] require the use of a suitable cost function for feature-enhanced SAR imaging. As as result of the approach we developed for complex SAR imagery, we are able to apply the proposed method successfully on real data of natural scenes.

Fig. 7 shows the reconstruction results for a set of α_1 values comprised of $\{0.9, 0.8, 0.7, 0.6, 0.5, 0.2\}$. α_2 was selected as (1-α_1) in each case. We observe that for larger α_1 values, the sparse features are more strongly emphasized, along with accompanying speckle characteristics. Decreasing α_1, or equivalently increasing α_2, contributes to a better contiguity of smooth structures in the image, while improving the suppression of speckle noise. A selection of $\alpha_1 = 0.8$ results in a visual balance between the sparse and smooth structures, whereas decreasing α_1 causes a slight oversmoothing of edges and sharper features in the image. Thus, we have observed a graceful degradation of the desired features with variation of the parameters α_1 and α_2. A more thorough study on the sensitivity of sparsity-driven SAR imaging to the choice of hyperparameters, and methods for automatic parameter selection can be found in [30].

In our final set of experiments, we apply our reconstruction technique to data collected with SARPER. Data collection in spotlight mode [24] is followed by interpolation of Fourier domain samples from polar to a rectangular grid. The collected data are %56 oversampled in range direction. The reference image obtained by 2-D inverse Fourier transformation of all of the available data samples of size 5000×3500 is shown in Fig. 8. The vertical axis (5000 elements) depicts range direction, and the horizontal axis (3500 elements) depicts azimuth direction. Minimum-norm reconstruction, following a rectangular masking operation containing 3.2% of all reference samples in the Fourier space, is shown in Fig. 9. Fig. 10 better illustrates the effectiveness of the method in preserving features of sparsity and piecewise-smooth variation in magnitude, present in the complex SAR imagery. Figs. 11–13 show similarly obtained results for a different scene, also indicating the applicability of our technique to airborne SAR data with complex imagery of larger sizes, such as 5000×3500, as is of interest in practical systems. In both sets of examples, we can clearly see that the proposed approach is successful in enhancing point-like and piecewise-constant features in the reconstruction with the complex ADMM SAR imaging framework.

Next we analyse the computational performance of our proposed approach. That of C-SALSA, studied for real images, in comparison to NESTA can be found in [17]. For complex imaging, we compare our results to an equivalent unconstrained problem as follows. We evaluate the feature-enhanced reconstruction method (herein referred to as FERM) [9], for which the performance results are given in Table I. The FERM solution is obtained first for a particular choice of the regularization parameter, and the data fidelity error ϵ of the result is measured and given as input to our method. To obtain a fair comparison, we set the stopping criterion for ADMM to reach the same cost value as that of the FERM solution $\mathbf{x}_{fe}$, which is given by $\alpha_1 \|\mathbf{x}_{fe}\|_1 + \alpha_2 TV(|\mathbf{x}_{fe}|)$. We implemented both algorithms in Matlab. We used a mex function in Chambolle projection step of the algorithm. The results in Table I show that the proposed method requires less computation time and scales well with larger image dimensions, though our analysis of computation times is based on a single selection of the hyperparameter. The dimensions of the SAR images used in the comparisons in Table I are 512×512 for TerraSAR, and 1024×1024 for SARPER. Each iterative step of the FERM requires solving a linear system of unknowns equal to the number of pixels in the image. The solution of such a linear system in each iteration—even when using methods such as conjugate gradient—does not scale well with increasing image sizes, or is affected adversely by reduction in available amount of data, as the conditioning of the system becomes worse with less data. On the other hand, for the proposed method, the computational bottlenecks in each iteration are 2-D FFTs; and therefore the number of operations per iteration scales well, with $O(N \log N)$, with number of pixels N. Furthermore, the proposed method's computation time is less sensitive to the reduction of data. Therefore, the proposed method is more suitable for use with SAR images that are of interest in practice, especially in compressed sensing scenarios where the linear system associated with the measurement model is inherently ill-conditioned.

Fig. 8. Reference image from SARPER—airborne SAR system developed by ASELSAN.

Fig. 9. Minimum-norm reconstruction from 3.2% of reference samples in Fourier space.

Fig. 10. Reconstruction with the proposed method from 3.2% of reference samples in Fourier space.

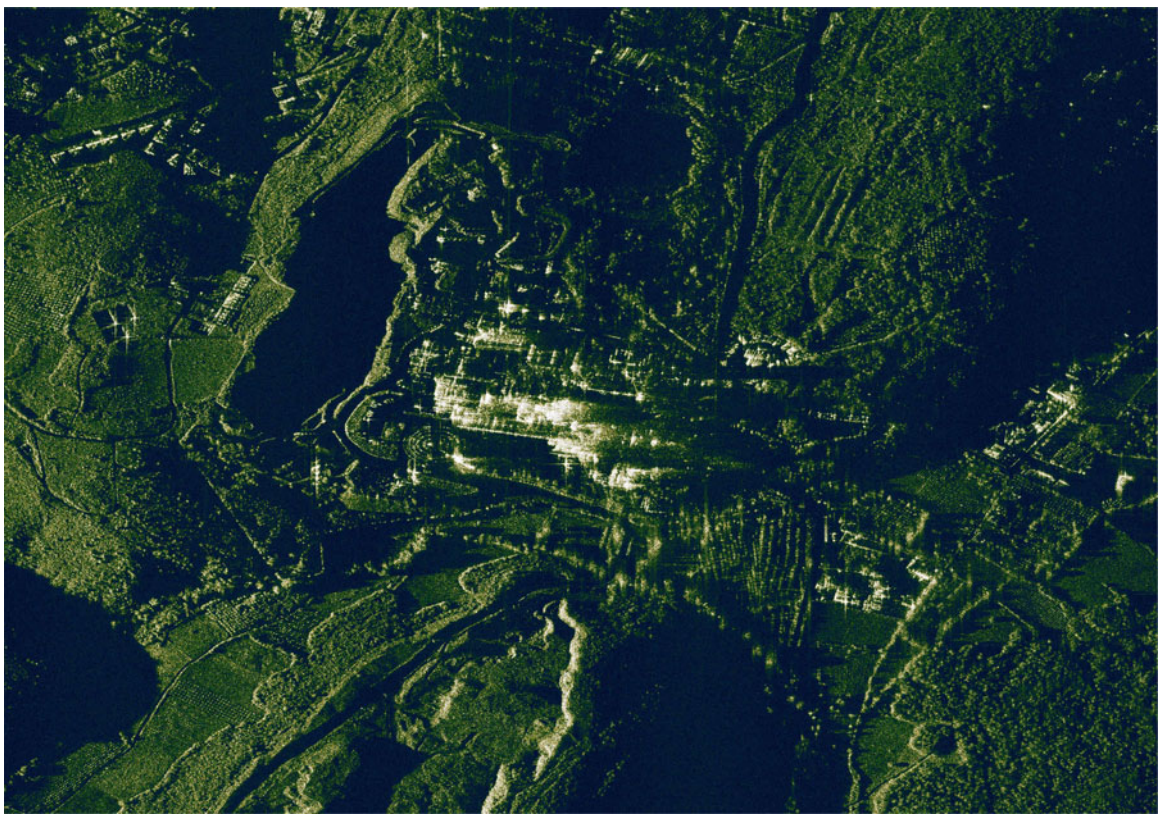

Fig. 11. Reference image from SARPER—airborne SAR system developed by ASELSAN.

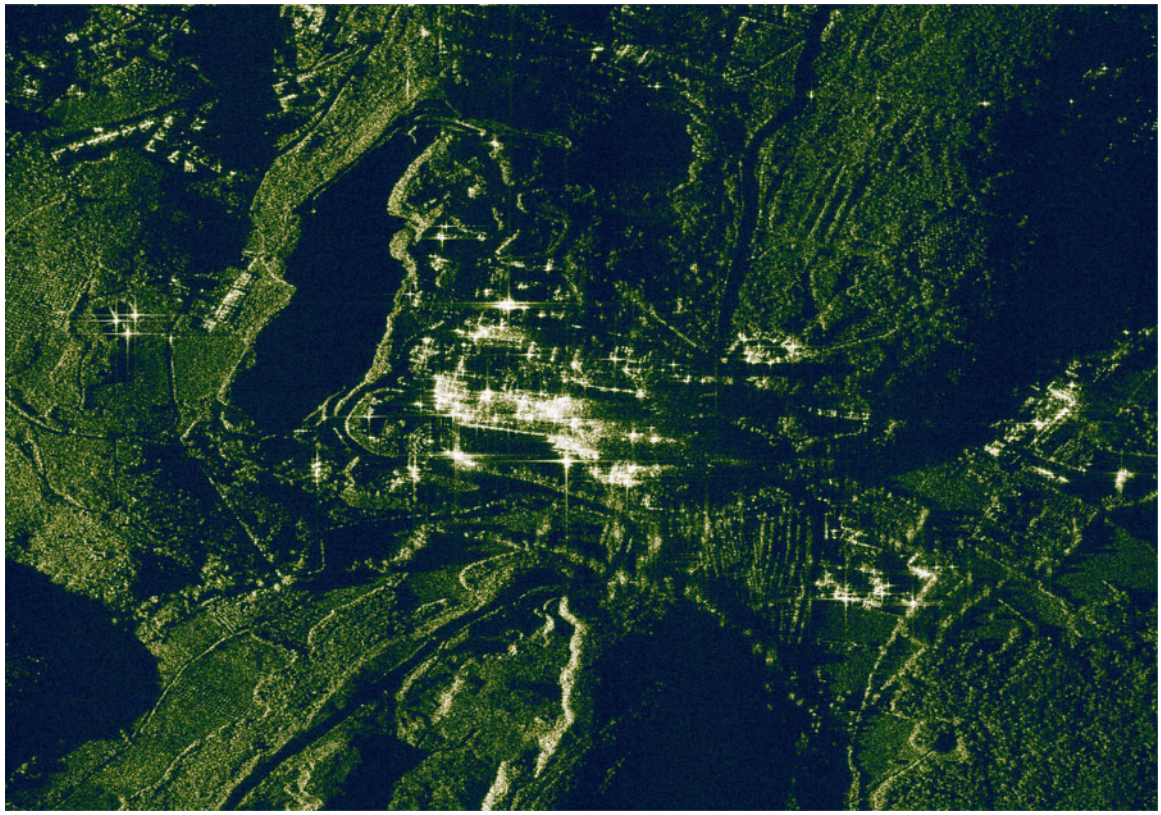

Fig. 12. Minimum-norm reconstruction from 3.2% of reference samples in Fourier space.

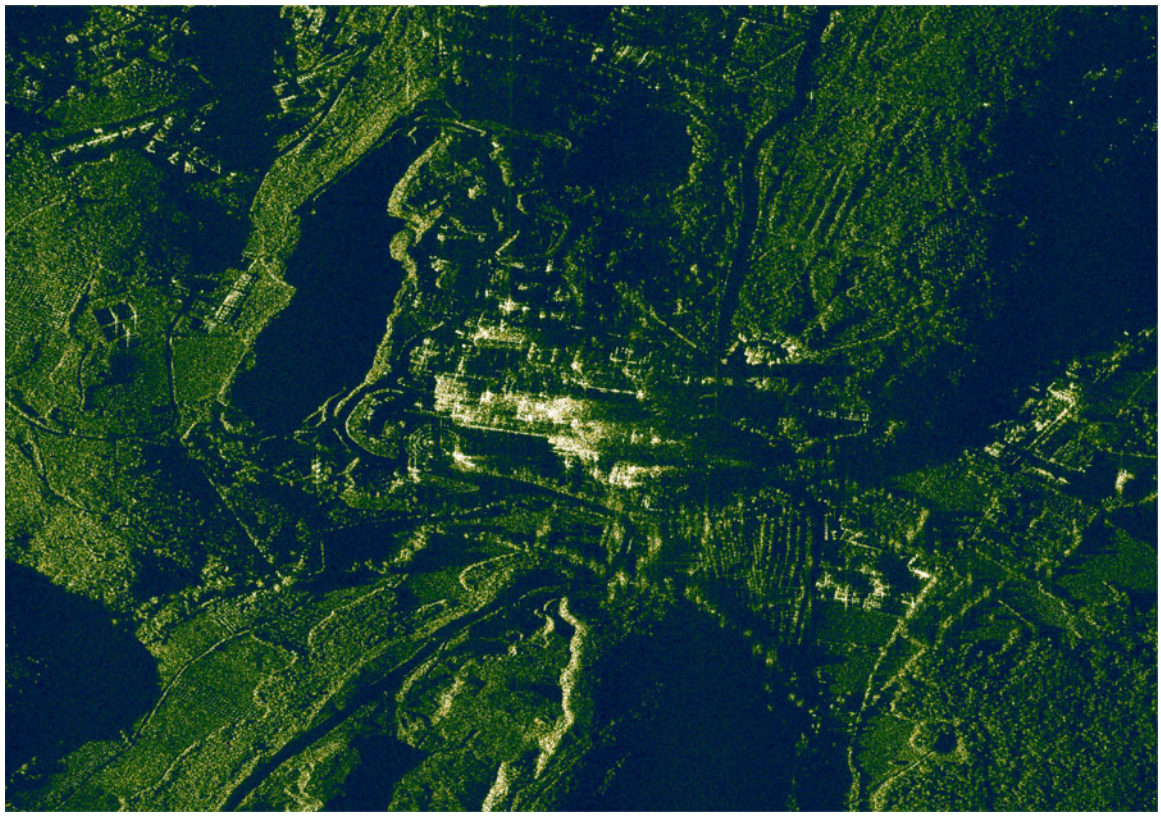

Fig. 13. Reconstruction with the proposed method from 3.2% of reference samples in Fourier space.

TABLE I
COMPUTATION TIMES, ERROR- AND COST-RATIOS FOR FERM AND HYBRID ADMM (AVERAGE COMPUTATION TIMES AND COST FUNCTION VALUES OVER 200 RUNS) WHERE N_{ADMM} REPRESENTS THE ADMM ITERATION COUNT

Data	Mask Type	Data Percentage	t_{FERM}	t_{ADMM}	N_{ADMM}	$\frac{\varepsilon_{\text{ADMM}}}{\varepsilon_{\text{FERM}}}$	$\frac{cost(x_{\text{ADMM}})}{cost(x_{\text{FERM}})}$
TerraSAR	Rectangular	75%	10.0 s	2.6 s	34	0.994	0.90
TerraSAR	Rectangular	50%	12.5 s	2.4 s	34	0.992	0.90
TerraSAR	Rectangular	25%	14.4 s	2.2 s	34	0.986	0.92
TerraSAR	Rectangular	11%	16.7 s	1.0 s	17	0.981	0.91
TerraSAR	Rectangular	6%	17.8 s	1.0 s	16	0.994	0.74
TerraSAR	Random	39%	12.4 s	2.7 s	38	0.957	0.90
TerraSAR	Random	22%	14.9 s	2.9 s	42	0.922	0.94
TerraSAR	Random	12%	17.6 s	3.0 s	47	0.909	0.90
TerraSAR	Random	6%	19.7 s	3.1 s	48	0.974	0.93
Sarper	Rectangular	75%	82.5 s	12.8 s	39	0.990	1.00
Sarper	Rectangular	50%	93.7 s	12.6 s	41	0.991	0.91
Sarper	Rectangular	25%	112.8 s	12.4 s	43	0.988	0.90
Sarper	Rectangular	11%	97.4 s	6.8 s	25	0.994	0.88
Sarper	Rectangular	6%	72.8 s	7.3 s	27	0.996	0.65
Sarper	Random	39%	99.4 s	13.2 s	42	0.989	0.98
Sarper	Random	22%	110.1 s	13.1 s	44	0.988	0.90
Sarper	Random	12%	113.4 s	12.8 s	45	0.985	0.94
Sarper	Random	6%	74.6 s	14.1 s	51	0.988	0.92

V. DISCUSSION

In this paper, we introduced an Augmented Lagrangian based approach for feature-enhanced / compressed SAR imaging. By rigorously deriving the proximal mappings for TV of the reflectivity magnitudes as well as for the 1-norm of a generic linear transformation of the reflectivity magnitudes, we were able to use an ADMM based technique that appropriately handles complex SAR imagery. We used the technique in conjunction with a hybrid cost function comprised of 1-norm and TV of reflectivity magnitudes, as is more appropriate for natural SAR images containing multiple types of features.. We were thus able to apply our ADMM-based method on complex-valued real SAR data from natural scenes. Our method is suitable for use with large image sizes as the computational complexity scales well with increasing dimensionality, as is typically desired in practical systems.

We validated our approach using raw data collected using SARPER—airborne SAR system developed by ASELSAN—as well as controlled numerical examples and images from TerraSAR to study the effectiveness of the proposed approach. Our results illustrate the computational benefits of using the proposed ADMM for complex SAR imaging, besides proving its feasibility with real SAR imagery of moderately large dimensions, with measurements obtained using SARPER.

An important aspect in SAR imaging is autofocusing [24], also in the context of compressed sensing [41]–[43]. Future efforts will focus on robustness to phase noise and other modeling imperfections to complement the work presented in this paper.

APPENDIX A
PROOF OF THEOREM 1: PROXIMAL MAPPING ASSOCIATED WITH THE 1-NORM OF A REAL VALUED LINEAR TRANSFORM OF MAGNITUDE FOR COMPLEX IMAGES

Theorem 1: Let $\phi(\mathbf{x}) = \|\mathbf{W}|\mathbf{x}|\|_1$ for $\mathbf{x} \in \mathbf{C}^N$, then $\text{prox}_{\phi}(\mathbf{v}) = \text{prox}_{\|\mathbf{W}\mathbf{x}\|_1}(|\mathbf{v}|)\cdot\exp\{\text{j}\angle(\mathbf{v})\}$.

Proof. First, define $\mathbf{x}$ and $\mathbf{v}$ as:

$$\mathbf{x} = \mathbf{a} + \text{j}\mathbf{b} \;\text{ and }\; \mathbf{v} = \mathbf{c} + \text{j}\mathbf{d}, \tag{35}$$

where $\mathbf{a}, \mathbf{b}, \mathbf{c}, \mathbf{d} \in \mathbf{R}^N$ and $\mathbf{W} \in \mathbf{R}^{N\times N}$. $\mathbf{W}[i,j]$ denotes the i,j-th element of the matrix $\mathbf{W}$, and $\mathbf{W}[i,:]$ denotes the row vector which consists of the elements of i-th row of the matrix $\mathbf{W}$. Let us continue with the definition of proximal mapping.

$$\begin{aligned}\text{prox}_{\phi}(\mathbf{v}) &= \arg\min_{\mathbf{x}} \; \phi(\mathbf{x}) + \frac{\mu}{2}\|\mathbf{x}-\mathbf{v}\|_2^2 \\ &= \arg\min_{\mathbf{a},\mathbf{b}} \sum_i \left| \sum_j \mathbf{W}[i,j]\sqrt{\mathbf{a}[j]^2 + \mathbf{b}[j]^2} \right| \quad (36) \\ &\quad + \sum_j \frac{\mu}{2}\left((\mathbf{a}[j]-\mathbf{c}[j])^2 + (\mathbf{b}[j]-\mathbf{d}[j])^2 \right). \quad (37)\end{aligned}$$

Taking partial derivatives with respect to both real and imaginary parts and equating each to zero vector gives the result as

$$\mathbf{a}[j] + \sum_i \frac{\mathbf{W}[i,j]\mathbf{a}[j]}{\mu|\mathbf{x}[j]|}\text{sign}(\mathbf{W}[i,:]|\mathbf{x}|) = \mathbf{c}[j], \tag{38}$$

$$\mathbf{b}[j] + \sum_i \frac{\mathbf{W}[i,j]\mathbf{b}[j]}{\mu|\mathbf{x}[j]|}\text{sign}(\mathbf{W}[i,:]|\mathbf{x}|) = \mathbf{d}[j]. \tag{39}$$

Summing Eqs. (38) and (39) multiplied with complex j side by side yields:

$$\begin{aligned}&\mathbf{a}[j] + \text{j}\mathbf{b}[j] + \sum_i \frac{\mathbf{W}[i,j](\mathbf{a}[j] + \text{j}\mathbf{b}[j])}{\mu|\mathbf{x}[j]|}\text{sign}(\mathbf{W}[i,:]|\mathbf{x}|) \\ &\quad = \mathbf{c}[j] + \text{j}\mathbf{d}[j], \end{aligned} \tag{40}$$

$$\mathbf{x}[j] + \sum_i \frac{\mathbf{W}[i,j]\mathbf{x}[j]}{\mu|\mathbf{x}[j]|}\text{sign}(\mathbf{W}[i,:]|\mathbf{x}|) = \mathbf{v}[j], \tag{41}$$

$$\exp\{\text{j}\angle\mathbf{x}[j]\}\left(|\mathbf{x}[j]| + \sum_i \frac{\mathbf{W}[i,j]}{\mu}\text{sign}(\mathbf{W}[i,:]|\mathbf{x}|)\right) = \exp\{\text{j}\angle\mathbf{v}[j]\}|\mathbf{v}[j]|. \tag{42}$$

One can divide Eq. (42) into two as phase and magnitude:

$$\exp\{\text{j}\angle\mathbf{x}[j]\} = \exp\{\text{j}\angle\mathbf{v}[j]\}, \tag{43}$$

$$|\mathbf{x}[j]| + \sum_i \frac{\mathbf{W}[i,j]}{\mu}\text{sign}(\mathbf{W}[i,:]|\mathbf{x}|) = |\mathbf{v}[j]|. \tag{44}$$

Just as easily one can derive proximal mapping for the real valued counterpart $\phi_r = \|\mathbf{W}\mathbf{x}\|_1$ as:

$$\text{prox}_{\phi_r}(\mathbf{v}) = \arg\min_{\mathbf{x}} \phi_r(\mathbf{x}) + \frac{\mu}{2}\|\mathbf{x}-\mathbf{v}\|_2^2, \tag{45}$$

$$= \arg\min_{\mathbf{x}} \sum_i \left|\sum_j \mathbf{W}[i,j]\mathbf{x}[j]\right| + \sum_j \frac{\mu}{2}\left(\mathbf{x}[j]-\mathbf{v}[j]\right)^2. \tag{46}$$

Same as before, taking partial derivative with respect to $\mathbf{x}$ and equating it to zero vector gives the result:

$$\mathbf{x}[j] + \sum_i \frac{\mathbf{W}[i,j]}{\mu}\text{sign}(\mathbf{W}[i,:]\mathbf{x}) = \mathbf{v}[j]. \tag{47}$$

If the input is positive valued, i.e. all elements of the vector $\mathbf{v}$ is positive, then the left side of the equation must also be positive. Therefore the result $\mathbf{x}$ must have all positive valued elements. Therefore for an input of $|\mathbf{v}|$, the output of the proximal mapping function is as follows:

$$|\mathbf{x}[j]| + \sum_i \frac{\mathbf{W}[i,j]}{\mu}\text{sign}(\mathbf{W}[i,:]|\mathbf{x}|) = |\mathbf{v}[j]|. \tag{48}$$

Eqs. (44) and (48) are exactly the same. Moreover, the phase of the input must be equal to the phase of the output. Therefore the following equality holds for any real valued linear transform over x.

$$\text{prox}_{\|\mathbf{W}|\mathbf{x}|\|_1}(\mathbf{v}) = \text{prox}_{\|\mathbf{W}\mathbf{x}\|_1}(|\mathbf{v}|)\cdot\exp\{\text{j}\angle(\mathbf{v})\}. \tag{49}$$

This concludes the proof of Theorem 1. ■

Appendix B
Proof of Theorem 2: Proximal Mapping Associated With the Magnitude-Total-Variation for Complex Images

Let us start with the definition of the proximal mapping associated with the TV:

$$\text{prox}_{TV}(\mathbf{v}) = \arg\min_{\mathbf{x}} TV(\mathbf{x}) + \frac{\mu}{2}\|\mathbf{x}-\mathbf{v}\|_2^2. \tag{50}$$

We are going to use two lemmas for our final proof.

Lemma 1: Let $|\angle(\mathbf{v}[i,j])| = |\angle(\text{prox}_{TV}(\mathbf{v})[i,j])|$ for all i,j. Then, the condition $\angle(\mathbf{v}[i,j]) = \angle(\text{prox}_{TV}(\mathbf{v})[i,j])$ holds for the minimizer $\mathbf{v} = \arg\min_{\mathbf{x}} TV(\mathbf{x}) + \frac{\mu}{2}\|\mathbf{x}-\mathbf{v}\|_2^2$.

Proof. If $|\angle(\mathbf{v}[i,j])| = |\angle(\text{prox}_{TV}(\mathbf{v})[i,j])|$, then either $\angle(\mathbf{v}[i,j]) = \angle(\text{prox}_{TV}(\mathbf{v})[i,j])$ or $\angle(\mathbf{v}[i,j]) = -\angle(\text{prox}_{TV}(\mathbf{v})[i,j])$. Since we are operating on the intensity (absolute value) of the pixels, neither of the choices affect the first term. We need to check how the two choices affect the second term, $\|\mathbf{x}-\mathbf{v}\|_2^2$, where $\mathbf{x} = \text{prox}_{TV}(\mathbf{v})$. We can simplify this operation as below:

$$\text{minimize}\sum_{i,j}\left|\begin{array}{c}|\mathbf{x}[i,j]|\exp\{\text{j}\angle(\mathbf{x}[i,j])\}\\ -|\mathbf{v}[i,j]|\exp\{\text{j}\angle(\mathbf{v}[i,j])\}\end{array}\right|^2. \tag{51}$$

If $\angle(\mathbf{v}[i,j]) = -\angle(\text{prox}_{TV}(\mathbf{v})[i,j])$, then for each i,j pair, the terms inside the summation is equal to

$$\text{minimize}\sum_{i,j}\left(|\mathbf{x}[i,j]| + |\mathbf{v}[i,j]|\right)^2, \tag{52}$$

whereas for $\angle(\mathbf{v}[i,j]) = \angle(\text{prox}_{TV}(\mathbf{v})[i,j])$, for each i,j the term is equal to

$$\text{minimize}\sum_{i,j}\left(|\mathbf{x}[i,j]| - |\mathbf{v}[i,j]|\right)^2. \tag{53}$$

It is obvious that the absolute value of the sum of two non-negative numbers as in Eq. (52) is greater than or equal to the absolute value of the difference of the two non-negative numbers as in (53). Therefore, setting $\angle(\mathbf{v}[i,j]) = \angle(\text{prox}_{TV}(\mathbf{v})[i,j])$ when $|\angle(\mathbf{v}[i,j])| = |\angle(\text{prox}_{TV}(\mathbf{v})[i,j])|$ ensures the minimization of each term in the summation in (51), and thus the sum itself. ■

Lemma 2: For a real image vector $\mathbf{a}\in\mathbf{R}^N$, $\min(\text{prox}_{TV}(\mathbf{a})) \geq \min(\mathbf{a})$.

Proof. We will use proof by contradiction. Let $\mathbf{p} = \text{prox}_{TV}(\mathbf{a})$, and i',j' denote the index values corresponding to the minimum value of the image vector $\mathbf{a}$. Assume that $\mathbf{p}[i',j'] < \mathbf{a}[i',j']$. Then, either (i) $\|\nabla\mathbf{p}\|_1 > \|\nabla\mathbf{a}\|_1$ or (ii) $\mathbf{p}[i,j] - \mathbf{a}[i,j] = c > 0$ for all $[i,j]$, for some $c\in\mathbf{R}$. For case (i), $TV(\mathbf{p}) > TV(\mathbf{a})$ and $\|\mathbf{p}-\mathbf{a}\|_2^2 > 0$; therefore $\mathbf{p}$ is not the minimizer of the cost function associated with the proximal mapping shown in (50). For case (ii), $TV(\mathbf{p}) = TV(\mathbf{a})$ and $\|\mathbf{p}-\mathbf{a}\|_2^2 = N\cdot c^2 > 0$; therefore, again, $\mathbf{p}$ is not the minimizer of the cost function of the proximal mapping operator. However, both cases (i) and (ii) lead to a contradiction. Hence, we conclude that $\min(\mathbf{p}) \geq \min(\mathbf{a})$ is always satisfied for $\mathbf{p} = \text{prox}_{TV}(\mathbf{a})$. ■

Theorem 2: Let $\phi(\mathbf{x}) = TV(|\mathbf{x}|)$. Then, $\text{prox}_{TV(|\cdot|)}(\mathbf{v})[i,j] = \text{prox}_{TV}(|\mathbf{v}|)[i,j]\cdot\exp\{\text{j}\angle(\mathbf{v}[i,j])\}$, where $\text{prox}_{TV}(\cdot)$ is the proximal mapping for the TV function $TV(\mathbf{x})$.

Proof. First, define $\mathbf{x}$ and $\mathbf{v}$ as:

$$\mathbf{x} = \mathbf{a} + \text{j}\mathbf{b}, \tag{54}$$

$$\mathbf{v} = \mathbf{c} + \text{j}\mathbf{d}. \tag{55}$$

Let us continue with the definition of the magnitude-Total-Variation:

$$TV\left(|\mathbf{x}|\right)=\sum_{i,j}\nabla|\mathbf{x}|[i,j] \tag{56}$$

Rewriting for the complex case, the associated proximal mapping becomes:

$$\begin{aligned}\mathrm{prox}_{TV\left(|\cdot|\right)}(\mathbf{v})=\arg\min_{\mathbf{a},\mathbf{b}}\sum_{i,j}\nabla\left(\sqrt{\mathbf{a}[i,j]^2+\mathbf{b}[i,j]^2}\right)\\ +\frac{\mu}{2}\left((\mathbf{a}[i,j]-\mathbf{c}[i,j])^2+(\mathbf{b}[i,j]-\mathbf{d}[i,j])^2\right).\end{aligned} \tag{57}$$

Let

$$\nabla_1\left(\sqrt{\mathbf{a}[i,j]^2+\mathbf{b}[i,j]^2}\right)=\mathbf{e}[i,j]=|\mathbf{x}[i,j]|-|\mathbf{x}[i-1,j]|, \tag{58}$$

$$\nabla_2\left(\sqrt{\mathbf{a}[i,j]^2+\mathbf{b}[i,j]^2}\right)=\mathbf{f}[i,j]=|\mathbf{x}[i,j]|-|\mathbf{x}[i,j-1]|. \tag{59}$$

Now the proximal mapping becomes:

$$\begin{aligned}\mathrm{prox}_{TV\left(|\cdot|\right)}(\mathbf{v})=\arg\min_{\mathbf{a},\mathbf{b}}\sum_{i,j}\sqrt{\mathbf{e}[i,j]^2+\mathbf{f}[i,j]^2}\\ +\frac{\mu}{2}((\mathbf{a}[i,j]-\mathbf{c}[i,j])^2+(\mathbf{b}[i,j]-\mathbf{d}[i,j])^2).\end{aligned} \tag{60}$$

Taking derivatives with respect to both real and imaginary parts, and setting them equal to zero yields the result. Beginning with the real part:

$$\begin{aligned}&\frac{\partial\sqrt{\mathbf{e}[i,j]^2+\mathbf{f}[i,j]^2}}{\partial\mathbf{a}[i,j]}+\frac{\partial\sqrt{\mathbf{e}[i+1,j]^2+\mathbf{f}[i+1,j]^2}}{\partial\mathbf{a}[i,j]}\\ &+\frac{\partial\sqrt{\mathbf{e}[i,j+1]^2+\mathbf{f}[i,j+1]^2}}{\partial\mathbf{a}[i,j]}+\mu(\mathbf{a}[i,j]-\mathbf{c}[i,j])\ =0,\end{aligned} \tag{61}$$

$$\begin{aligned}&\frac{\mathbf{a}[i,j]}{|\mathbf{x}[i,j]|}\left(\mu|\mathbf{x}[i,j]|+\frac{\mathbf{e}[i,j]+\mathbf{f}[i,j]}{\sqrt{\mathbf{e}[i,j]^2+\mathbf{f}[i,j]^2}}\right.\\ &\left.+\frac{-\mathbf{e}[i+1,j]}{\sqrt{\mathbf{e}[i+1,j]^2+\mathbf{f}[i+1,j]^2}}+\frac{-\mathbf{f}[i,j+1]}{\sqrt{\mathbf{e}[i,j+1]^2+\mathbf{f}[i,j+1]^2}}\right)\\ &=\mu\mathbf{c}[i,j].\end{aligned} \tag{62}$$

Likewise, for the imaginary part:

$$\begin{aligned}&\frac{\partial\sqrt{\mathbf{e}[i,j]^2+\mathbf{f}[i,j]^2}}{\partial\mathbf{b}[i,j]}+\frac{\partial\sqrt{\mathbf{e}[i+1,j]^2+\mathbf{f}[i+1,j]^2}}{\partial\mathbf{b}[i,j]}\\ &+\frac{\partial\sqrt{\mathbf{e}[i,j+1]^2+\mathbf{f}[i,j+1]^2}}{\partial\mathbf{b}[i,j]}+\mu(\mathbf{b}[i,j]-\mathbf{d}[i,j])=0,\end{aligned} \tag{63}$$

$$\begin{aligned}&\frac{\mathbf{b}[i,j]}{|\mathbf{x}[i,j]|}\left(\mu|\mathbf{x}[i,j]|+\frac{\mathbf{e}[i,j]+\mathbf{f}[i,j]}{\sqrt{\mathbf{e}[i,j]^2+\mathbf{f}[i,j]^2}}\right.\\ &\left.+\frac{-\mathbf{e}[i+1,j]}{\sqrt{\mathbf{e}[i+1,j]^2+\mathbf{f}[i+1,j]^2}}+\frac{-\mathbf{f}[i,j+1]}{\sqrt{\mathbf{e}[i,j+1]^2+\mathbf{f}[i,j+1]^2}}\right)\\ &=\mu\mathbf{d}[i,j].\end{aligned} \tag{64}$$

Dividing Eq. (64) by Eq. (62) side by side, we reach:

$$\frac{\mathbf{b}[i,j]}{\mathbf{a}[i,j]}=\frac{\mathbf{d}[i,j]}{\mathbf{c}[i,j]}. \tag{65}$$

The result above implies that $|\angle(\mathbf{v}[i,j])|=|\angle(\mathbf{x}[i,j])|$. By Lemma 1, we can say that $\angle(\mathbf{v}[i,j])=\angle(\mathbf{x}[i,j])$.

Multiplying (64) by j and summing with (62) yields:

$$\begin{aligned}&\frac{\mathbf{a}[i,j]+\mathrm{j}\mathbf{b}[i,j]}{|\mathbf{x}[i,j]|}\left(\mu|\mathbf{x}[i,j]|+\frac{\mathbf{e}[i,j]+\mathbf{f}[i,j]}{\sqrt{\mathbf{e}[i,j]^2+\mathbf{f}[i,j]^2}}\right.\\ &\left.+\frac{-\mathbf{e}[i+1,j]}{\sqrt{\mathbf{e}[i+1,j]^2+\mathbf{f}[i+1,j]^2}}+\frac{-\mathbf{f}[i,j+1]}{\sqrt{\mathbf{e}[i,j+1]^2+\mathbf{f}[i,j+1]^2}}\right)\\ &=\mu(\mathbf{c}[i,j]+\mathrm{j}\mathbf{d}[i,j]),\end{aligned} \tag{66}$$

$$\begin{aligned}&\frac{\mathbf{x}[i,j]}{|\mathbf{x}[i,j]|}\left(\mu|\mathbf{x}[i,j]|+\frac{\mathbf{e}[i,j]+\mathbf{f}[i,j]}{\sqrt{\mathbf{e}[i,j]^2+\mathbf{f}[i,j]^2}}\right.\\ &\left.+\frac{-\mathbf{e}[i+1,j]}{\sqrt{\mathbf{e}[i+1,j]^2+\mathbf{f}[i+1,j]^2}}+\frac{-\mathbf{f}[i,j+1]}{\sqrt{\mathbf{e}[i,j+1]^2+\mathbf{f}[i,j+1]^2}}\right)\\ &=\mu\mathbf{v}[i,j],\end{aligned} \tag{67}$$

$$\begin{aligned}&\exp\{\mathrm{j}\angle(\mathbf{x}[i,j])\}\left(\mu|\mathbf{x}[i,j]|+\frac{\mathbf{e}[i,j]+\mathbf{f}[i,j]}{\sqrt{\mathbf{e}[i,j]^2+\mathbf{f}[i,j]^2}}\right.\\ &\left.+\frac{-\mathbf{e}[i+1,j]}{\sqrt{\mathbf{e}[i+1,j]^2+\mathbf{f}[i+1,j]^2}}+\frac{-\mathbf{f}[i,j+1]}{\sqrt{\mathbf{e}[i,j+1]^2+\mathbf{f}[i,j+1]^2}}\right)\\ &=\mu\mathbf{v}[i,j],\end{aligned} \tag{68}$$

$$\begin{aligned}&\mu|\mathbf{x}[i,j]|+\frac{\mathbf{e}[i,j]+\mathbf{f}[i,j]}{\sqrt{\mathbf{e}[i,j]^2+\mathbf{f}[i,j]^2}}\\ &+\frac{-\mathbf{e}[i+1,j]}{\sqrt{\mathbf{e}[i+1,j]^2+\mathbf{f}[i+1,j]^2}}+\frac{-\mathbf{f}[i,j+1]}{\sqrt{\mathbf{e}[i,j+1]^2+\mathbf{f}[i,j+1]^2}}\\ &=\mu|\mathbf{v}[i,j]|.\end{aligned} \tag{69}$$

Next we consider the proximal mapping associated with the TV of a real valued input. Solving Eq. (61), by setting $\mathbf{b}=0$, $\mathbf{d}=0$, and defining:

$$\mathrm{prox}_{TV}(\mathbf{c})=\arg\min_{\mathbf{a}}\sum_{i,j}|\nabla\mathbf{a}|[i,j]+\frac{\mu}{2}(\mathbf{a}[i,j]-\mathbf{c}[i,j])^2, \tag{70}$$

and

$$\left(\nabla_1\mathbf{a}\right)[i,j]=\ \mathbf{e}'[i,j]=\mathbf{a}[i,j]-\mathbf{a}[i-1,j], \tag{71}$$

$$\left(\nabla_2\mathbf{a}\right)[i,j]=\ \mathbf{f}'[i,j]=\mathbf{a}[i,j]|-\mathbf{a}[i,j-1]. \tag{72}$$

Taking derivative of Eq. (70) with respect to $\mathbf{a}$ yields as in Eq. (61):

$$\begin{aligned}&\frac{\partial\sqrt{\mathbf{e}'[i,j]^2+\mathbf{f}'[i,j]^2}}{\partial\mathbf{a}[i,j]}+\frac{\partial\sqrt{\mathbf{e}'[i+1,j]^2+\mathbf{f}'[i+1,j]^2}}{\partial\mathbf{a}[i,j]}\\ &+\frac{\partial\sqrt{\mathbf{e}'[i,j+1]^2+\mathbf{f}'[i,j+1]^2}}{\partial\mathbf{a}[i,j]}+\mu(\mathbf{a}[i,j]-\mathbf{c}[i,j])=0,\end{aligned} \tag{73}$$

$$\mu\mathbf{a}[i,j] + \frac{\mathbf{e}'[i,j] + \mathbf{f}'[i,j]}{\sqrt{\mathbf{e}'[i,j]^2 + \mathbf{f}'[i,j]^2}} + \frac{-\mathbf{e}'[i+1,j]}{\sqrt{\mathbf{e}'[i+1,j]^2 + \mathbf{f}'[i+1,j]^2}} + \frac{-\mathbf{f}'[i,j+1]}{\sqrt{\mathbf{e}'[i,j+1]^2 + \mathbf{f}'[i,j+1]^2}} = \mu\mathbf{c}[i,j]. \quad (74)$$

At this point we use Lemma 2 to reach the following statement. When all elements of the input image are non-negative, the proximal mapping associated with the TV function will result in an output image with non-negative elements only.

Next, let the input of $\text{prox}_{TV}(\cdot)$ be $|\mathbf{v}|$, which is populated with non-negative real elements only. Then the output $\mathbf{a}'$ has only non-negative elements. Setting $\mathbf{x}'[i,j] = |\mathbf{x}'[i,j]|$ in Eq. (74), we get:

$$\mu|\mathbf{x}'[i,j]| + \frac{\mathbf{e}[i,j] + \mathbf{f}[i,j]}{\sqrt{\mathbf{e}[i,j]^2 + \mathbf{f}[i,j]^2}} + \frac{-\mathbf{e}[i+1,j]}{\sqrt{\mathbf{e}[i+1,j]^2 + \mathbf{f}[i+1,j]^2}} + \frac{-\mathbf{f}[i,j+1]}{\sqrt{\mathbf{e}[i,j+1]^2 + \mathbf{f}[i,j+1]^2}} = \mu|\mathbf{v}'[i,j]|. \quad (75)$$

The resulting equation is exactly the same as (69). Thus, we reach the result:

$$\text{prox}_{TV}(|\mathbf{v}|)[i,j] = \mathbf{x}'[i,j] = |\mathbf{x}[i,j]| = \left|\text{prox}_{TV(|\cdot|)}(\mathbf{v})[i,j]\right|. \quad (76)$$

Equation (65), together with Lemma 1, implies preservation of the phase $\angle(\mathbf{v}[i,j])$. Hence, we reach the following result:

$$\text{prox}_{TV(|\cdot|)}(\mathbf{v})[i,j] = \text{prox}_{TV}(|\mathbf{v}|)[i,j] \cdot \exp\{\text{j}\angle(\mathbf{v}[i,j])\} \quad \text{such that } \phi(\mathbf{x}) = \text{TV}(|\mathbf{x}|). \quad (77)$$

that is the argument of Theorem 2.

REFERENCES

[1] J. Ender, "On compressive sensing applied to radar," *Signal Process.*, vol. 90, no. 5, pp. 1402–1414, May 2010.

[2] L. C. Potter, E. Ertin, J. T. Parker, and M. Çetin, "Sparsity and compressed sensing in radar imaging," *Proc. IEEE*, vol. 98, no. 6, pp. 1006–1020, Jun. 2010.

[3] V. M. Patel, G. R. Easley, D. M. Healy Jr., and R. Chellappa, "Compressed synthetic aperture radar," *IEEE J. Sel. Topics Signal Process.*, vol. 4, no. 2, pp. 244–254, Apr. 2010.

[4] M. Cetin *et al.*, "Sparsity-driven synthetic aperture radar imaging: Reconstruction, autofocusing, moving targets, and compressed sensing," *IEEE Signal Process. Mag.*, vol. 31, no. 4, pp. 27–40, Jul. 2014.

[5] S. Samadi, M. Çetin, and M. A. Masnadi-Shirazi, "Sparse representation-based synthetic aperture radar imaging," *IET Radar, Sonar Navigat.*, vol. 5, no. 2, pp. 182–193, Feb. 2011.

[6] J. H. G. Ender, "A brief review of compressive sensing applied to radar," in *Proc. 14th Int. Radar Symp.*, Dresden, Germany, Jun. 2013, pp. 3–16.

[7] J. H. G. Ender, "Autofocusing ISAR images via sparse representation," in *Proc. 9th Eur. Conf. Synthetic Aperture Radar*, Nuremberg, Germany, Apr. 2012, pp. 203–206.

[8] R. Baraniuk and P. Steeghs, "Compressive radar imaging," in *Proc. IEEE Radar Conf.*, Boston, MA, USA, Apr. 2007, pp. 128–133.

[9] M. Cetin and W. C. Karl, "Feature-enhanced synthetic aperture radar image formation based on nonquadratic regularization," *IEEE Trans. Image Process.*, vol. 10, no. 4, pp. 623–631, Apr. 2001.

[10] E. van den Berg and M. P. Friedlander, "Probing the Pareto Frontier for basis pursuit solutions," *SIAM J. Sci. Comp*, vol. 31, no. 2, pp. 890–912, 2009.

[11] Z. Wang and W. Wang, "Fast and adaptive method for SAR superresolution imaging based on point scattering model and optimal basis selection," *IEEE Trans. Image Process.*, vol. 18, no. 7, pp. 1477–1486, Jul. 2009.

[12] M. Ferrara, J. A. Jackson, and C. Austin, "Enhancement of multi-pass 3D circular SAR images using sparse reconstruction techniques," *Proc. SPIE Algorithms Synthetic Aperture Radar Imagery XVI*, vol. 7337, Apr. 2009, Art. no. 733702

[13] M. Davies, G. Rilling, and T. Blumensath, "Greedy algorithms for compressed sensing," in *Compressed Sensing : Theory and Applications*, Y. Eldar & G. Kutyniok eds. Cambridge, U.K.: Cambridge Univ. Press, 2012, pp. 348–393.

[14] S. Boyd, N. Parikh, E. Chu, B. Peleato, and J. Eckstein, "Distributed optimization and statistical learning via the alternating direction method of multipliers," *Foundations Trends Mach. Learning*, vol. 3, no. 1, pp. 1–122, 2011.

[15] S. Wright, R. Nowak, and M. Figueiredo, "Sparse reconstruction by separable approximation," *IEEE Trans. Signal Process.*, vol. 57, no. 7, pp. 2479–2493, Jul. 2009.

[16] M. Afonso, J. M. Bioucas-Dias, and M. A. T. Figueiredo, "Fast image recovery using variable splitting and constrained optimization," *IEEE Trans. Image Process.*, vol. 10, no. 9, pp. 2345–2356, Sep. 2010.

[17] M. Afonso, J. M. Bioucas-Dias, and M. A. T. Figueiredo, "An augmented Lagrangian approach to the constrained optimization formulation of imaging inverse problems," *IEEE Trans. Image Process.*, vol. 20, no. 3, pp. 681–695, Mar. 2011.

[18] M. Annergren, A. Hansson, and B. Wahlberg, "An ADMM algorithm for solving ℓ_1 regularized MPC," in *Proc. IEEE 51st Conf. Decision Control*, Maui, HI, USA, Dec. 2012, pp. 4486–4491.

[19] B. Wahlberg, S. Boyd, M. Annergren, and Y. Wang, "An ADMM algorithm for a class of total variation regularized estimation problems," presented at the 16th IFAC Symp. System Identification, Brussels, Belgium, Jul. 2012.

[20] H. E. Guven and M. Cetin, "An augmented Lagrangian method for sparse SAR imaging," in *Proc. 10th Eur. Conf. Synthetic Aperture Radar*, Jun. 2014, pp. 1–4.

[21] H. E. Guven, A. Gungor, and M. Cetin, "An augmented Lagrangian method for image reconstruction with multiple features," in *Proc. IEEE Int. Conf. Image Process.*, Sep. 2015, pp. 4175–4179.

[22] Astrium TerraSAR-X sample imagery. [Online]. Available: http://www.astrium-geo.com/en/23-sample-imagery

[23] ASELSAN website for SARPER$^{\text{TM}}$. [Online]. Available: http://www.aselsan.com.tr/en-us/capabilities/radar-systems/

[24] C. V. Jakowatz, D. E. Wahl, P. S. Eichel, D. C. Ghiglia, and P. A. Thompson, *Spotlight-Mode Synthetic Aperture Radar: A Signal Processing Approach*. Norwell, MA, USA: Kluwer Academic, 1996.

[25] W. G. Carrara, R. S. Goodman, and R. M. Majewski, *Spotlight Synthetic Aperture Radar Signal Processing Algorithms*. Norwood, MA, USA: Artech House, 1995.

[26] M. Soumekh, *Synthetic Aperture Radar Signal Processing With MATLAB Algorithms*. Hoboken, NJ, USA: Wiley, 1999.

[27] D. C. Munson Jr., J. D. O'Brien, and W. K. Jenkins, "A tomographic formulation of spotlight-mode synthetic aperture radar," *Proc. IEEE*, vol. 71, no. 8, pp. 917–925, Aug. 1983.

[28] A. C. Kak and M. Slaney, *Principles of Computerized Tomographic Imaging*, vol. 1. Piscataway, NJ, USA: IEEE Press, Oct. 1992, pp. 505–517.

[29] J. M. Bioucas-Dias and M. A. T. Figueiredo, "Total variation restoration of speckled images using a Split-Bregman algorithm," *IEEE 16th Int. Conf. Image Process*, 2009, pp. 3717–3720.

[30] O. Batu and M. Çetin, "Parameter selection in sparsity-driven SAR imaging," *IEEE Trans. Aerosp. Electron. Syst.*, vol. 47, no. 4, pp. 3040–3050, Oct. 2011.

[31] G. H. Golub, M. Heath, and G. Wahba, "Generalized cross-validation as a method for choosing a good ridge parameter," *Technometrics*, vol. 21, no. 2, pp. 215–223, 1979.

[32] P. C. Hansen, "Analysis of discrete ill-posed problems by means of the L-curve," *SIAM Rev.*, vol. 34, no. 4, pp. 561–580, 1992.

[33] A. Chambolle, "Total variation minimization and a class of binary MRF models," *Energy Minimization Methods Comput. Vis. Pattern Recog.*, vol. 3757, pp. 136–152, 2005.

[34] A. Maleki, L. Anitori, Z. Yang, and R. Baraniuk, "Asymptotic analysis of complex LASSO via complex approximate message passing (CAMP)," *IEEE Trans. Inform. Theory.*, vol. 59, no. 7, pp. 4290–4308, Jul. 2013.

[35] D. Needell and R. Ward, "Near-Optimal compressed sensing guarantees for total variation minimization," *IEEE Trans. Image Process.*, vol. 22, no. 10, pp. 3941–3949, Oct. 2013.
[36] F. Zhao, D. C. Noll, J. F. Nielsen, and J. A. Fessler, "Separate magnitude and phase regularization via compressed sensing," *IEEE Trans. Med. Imag.*, vol. 31, no. 9, pp. 1713–1723, Sep. 2012.
[37] S. Samadi, M. Cetin, and M. A. M. Masnadi-Shirazi, "Multiple feature-enhanced SAR imaging using sparsity in combined dictionaries," *IEEE Geosc. Remote Sens. Lett.*, vol. 10, no. 4, pp. 821–825, Jul. 2013.
[38] R. L. Moses, L. Potter, and M. Çetin, "Wide angle SAR imaging," *Proc. SPIE*, vol. 5427, Apr. 2004.
[39] O. Teke, A. C. Gurbuz, and O. Arikan, "A robust compressive sensing based technique for reconstruction of sparse radar scenes," *Digit. Signal Process.*, vol. 27, pp. 23–32, 2014.
[40] I. Stojanovic, M. Cetin, and W. C. Karl, "Compressed sensing of monostatic and multistatic SAR," *IEEE Geosci. Remote Sens. Lett.*, vol. 10, no. 6, pp. 1444–1449, Nov. 2013.
[41] N. O. Onhon and M. Çetin, "A sparsity-driven approach for joint SAR imaging and phase error correction," *IEEE Trans. Image Process.*, vol. 21, no. 4, pp. 2075–2088, Apr. 2012.
[42] S. I. Kelly, M. Yaghoobi, and M. E. Davies, "Auto-focus for under-sampled synthetic aperture radar," in *Proc. Sensor Signal Process. Defence*, London, U.K., Sep. 2012, pp. 1–5.
[43] S. Ugur and O. Arikan, "SAR image reconstruction and autofocus by compressed sensing," *Digital Signal Process.*, vol. 22, no. 6, pp. 923–932, Dec. 2012.

H. Emre Güven received the B.Sc. and M.Sc. degree from Bilkent University, Ankara, Turkey, in 2003 and 2005, respectively, both in electrical and electronics engineering. He received the Ph.D. degree in electrical and computer engineering from Northeastern University, Boston, MA, USA, in 2012.

His experience includes positions as a Radar Systems Engineer and a Research Engineer. Since March 2014, he has been leading the Department of Advanced Sensing Research Programs, ASELSAN Research Center, Ankara. His research interests include signal and image processing, computational imaging, statistical estimation, and inverse problems. Applications in this context include radar, medical, and infrared imaging. He is a Member of Eta Kappa Nu.

Alper Güngör was born in Bursa, Turkey, in 1991. He received the B.Sc. degree (hons.) in the Department of Electrical and Electronics Engineering, Middle East Technical University (METU), Ankara, Turkey, in 2014, with a minor degree in information systems, computer engineering. He is currently working toward the M.Sc. degree in computer engineering at METU, and is also a Researcher in the Department of Advanced Sensing Research Programs, ASELSAN Research Center. His research interest includes compressed sensing, image reconstruction, and signal processing.

Müjdat Çetin (S'98–M'02) received the Ph.D. degree from Boston University, Boston, MA, USA, in 2001. From 2001 to 2005, he was with the Laboratory for Information and Decision Systems, Massachusetts Institute of Technology (MIT), Cambridge, MA. Since 2005, has been a Faculty Member at Sabancı University, Istanbul, Turkey. He has held visiting faculty positions at MIT, Northeastern University, Boston, and Boston University. He is currently an Associate Editor for the IEEE TRANSACTIONS ON COMPUTATIONAL IMAGING. He has been an Associate Editor for the IEEE TRANSACTIONS ON IMAGE PROCESSING, the IEEE Signal Processing Letters, and the IEEE TRANSACTIONS ON CYBERNETICS; a Guest Editor for Pattern Recognition Letters; and an Area Editor for the *Journal of Advances in Information Fusion*. He served as the Technical Program Cochair for the IEEE Image, Video, and Multidimensional Signal Processing Workshop in 2016; the International Conference on Information Fusion in 2013 and 2016; the International Conference on Pattern Recognition in 2010; and the IEEE Turkish Conference on Signal Processing, Communications, and their Applications in 2006. He was one of the keynote speakers for the 2015 International Workshop on Compressed Sensing Theory and its Applications to Radar, Sonar, and Remote Sensing. He was the 2010 IEEE Signal Processing Society Best Paper Award; the 2007 EURASIP/Elsevier Signal Processing Best Paper Award; the 2013 IET Radar, Sonar and Navigation Premium (Best Paper) Award; and the 2008 Turkish Academy of Sciences Distinguished Young Scientist Award. His research interests include the field of statistical signal processing, and include computational imaging, sparse signal and image representation, brain-computer interfaces, biomedical image analysis, and image segmentation.